JAMES | Journal of Advances in Modeling Earth Systems

RESEARCH ARTICLE
10.1029/2021MS002619

From Sugar to Flowers: A Transition of Shallow Cumulus Organization During ATOMIC

Pornampai Narenpitak[1,2], Jan Kazil[1,2], Takanobu Yamaguchi[1,2], Patricia Quinn[3], and Graham Feingold[2]

[1]Cooperative Institute for Research in Environmental Sciences, University of Colorado Boulder, Boulder, CO, USA, [2]National Oceanic and Atmospheric Administration, Chemical Sciences Laboratory, Boulder, CO, USA, [3]National Oceanic and Atmospheric Administration, Pacific Marine Environmental Laboratory, Seattle, WA, USA

Key Points:

- Lagrangian large eddy simulation can reproduce the transition of shallow cumulus organization from sugar to flowers observed on February 2–3, 2020 during Atlantic Tradewind Ocean-Atmosphere Mesoscale Interaction Campaign
- While large-scale upward vertical wind deepens the cloud layer, mesoscale wind renders moist areas moister assisting cloud organization
- Stronger large-scale upward motion strengthens the mesoscale circulation and accelerates the sugar-to-flowers transition process

Supporting Information:

Supporting Information may be found in the online version of this article.

Correspondence to:

P. Narenpitak,
pornampai.narenpitak@noaa.gov

Citation:

Narenpitak, P., Kazil, J., Yamaguchi, T., Quinn, P., & Feingold, G. (2021). From sugar to flowers: A transition of shallow cumulus organization during ATOMIC. *Journal of Advances in Modeling Earth Systems*, *13*, e2021MS002619. https://doi.org/10.1029/2021MS002619

Received 9 JUN 2021
Accepted 13 SEP 2021

Abstract The Atlantic Tradewind Ocean-Atmosphere Mesoscale Interaction Campaign (ATOMIC) took place in January–February, 2020. It was designed to understand the relationship between shallow convection and the large-scale environment in the trade-wind regime. A Lagrangian large eddy simulation, following the trajectory of a boundary-layer airmass, can reproduce a transition of trade cumulus organization from "sugar" to "flower" clouds with cold pools, observed on February 2–3. The simulation is driven with reanalysis large-scale meteorology, and in-situ aerosol data from ATOMIC and its joint field study EUREC^{4}A. During the transition, large-scale upward motion deepens the cloud layer. The total water path and optical depth increase, especially in the moist regions where flowers aggregate. This is due to mesoscale circulation that renders a net convergence of total water in the already moist and cloudy regions, strengthening the organization. An additional simulation shows that stronger large scale upward motion reinforces the mesoscale circulation and accelerates the organization process by strengthening the cloud-layer mesoscale buoyant turbulence kinetic energy production.

Plain Language Summary Fair-weather shallow clouds have different sizes and cloud properties. A field study called the Atlantic Tradewind Ocean-Atmosphere Mesoscale Interaction Campaign (ATOMIC) and Elucidating the Role of Clouds-Circulation Coupling in Climate (EUREC^{4}A) was designed to further understand the properties of these clouds. On February 2–3, very small and shallow "sugar" clouds grow into wider and deeper "flower" cloud clusters, no more than 3 km high. The clear spaces between the clouds expand. This study finds that local air circulation is responsible for making the moist and cloudy areas moister, and dry and cloud-free areas drier, enabling a process responsible for this transition. The large-scale vertical winds modulate the rate and strength of this process, which occurs locally at smaller scales.

1. Introduction

Low-level clouds forming in the warm marine boundary layer continue to be a leading source of uncertainty in global climate models (i.e., Bony & Dufresne, 2005; Boucher et al., 2013; Zelinka et al., 2016). Challenges associated with the study of these clouds include resolving the internal cloud processes at a fine scale while maintaining an accurate representation of the meteorology in which the clouds occur. The time scale and seasonality are also important, as summertime and wintertime shallow cumuli observed from the same oceanic regions may exhibit different characteristics (Lamer et al., 2015; Nuijens et al., 2014, 2015; Vogel et al., 2020).

Previous studies have used high-resolution simulations and satellite retrievals to help understand the relationships between shallow cumulus properties and the large-scale atmospheric and oceanic conditions. For example, the Barbados Oceanographic and Meteorological Experiment (BOMEX) (Holland & Rasmusson, 1973) examined the turbulent dynamics of summertime shallow cumuli in the Atlantic Ocean using different large eddy simulation (LES) models (Siebesma et al., 2003). The cloud feedback model intercomparison project—global atmospheric system study intercomparison of large eddy models and single column models (CGILS) investigated the mechanisms of cloud feedback of shallow cumulus and stratocumulus under idealized climate change perturbations based on summertime subtropical atmospheric conditions in the Pacific Ocean (Bretherton et al., 2013; Blossey et al., 2013; Zhang et al., 2013). Bretherton and Blossey (2017)

(referred to as BB2017 for short) further explored a mechanism of shallow cumulus organization in different large-scale conditions, including those from BOMEX and one of the CGILS cases. Organization of precipitating shallow cumulus clouds in the presence of cold pools during the Rain in Cumulus over the Ocean (RICO) (Rauber et al., 2007) has been studied with LES by vanZanten et al. (2011), Seifert and Heus (2013), Zuidema et al. (2017), and the references therein. In addition, Mieslinger et al. (2019) examined how different meteorological conditions affect cloud properties across different oceanic basins using high-resolution satellite imagery.

Other studies have used LES models to explore cloud processes that require finer representation of shallow cumuli. For instance, Vial et al. (2019) found that the cloudiness of wintertime North Atlantic trade shallow cumuli is sensitive to the diurnal cycle, both for nonprecipitating and precipitating clouds. Vogel et al. (2020) found that trade cumuli with stratiform cloudiness forming downstream of the trade wind region are tightly controlled by the inversion strength, deepening of the cloud layer, and longwave radiative cooling. Narenpitak and Bretherton (2019) used LES with forcings derived from the trade wind region of an idealized aquaplanet cloud-resolving model to explore the response of shallow cumulus in a warmer climate, and found that radiative cooling and free-tropospheric humidity are keys to controlling the cloudiness in their simulations. The use of in-situ observations, high-resolution simulations and remote sensing tools over the years have enabled studies that lead to better understanding of shallow cumulus processes.

A field campaign designed to study shallow convection in the trade wind region occurred in January–February, 2020 in the Atlantic Ocean east of Barbados. The Atlantic Tradewind Ocean-Atmosphere Mesoscale Interaction Campaign (ATOMIC) and its European counterpart called Elucidating the Role of Clouds-Circulation Coupling in Climate (EUREC^{4}A) formed a field campaign that used instruments on research aircrafts and ships to observe the properties of shallow cumulus clouds in order to better understand their relationship with the large-scale environment (Bony et al., 2017; Pincus et al., 2021; Quinn et al., 2020; Stevens et al., 2021). Recent studies (i.e., Bony et al., 2020; Rasp et al., 2020; Stevens et al., 2020) have categorized the mesoscale organization of shallow cumuli based on the Moderate Resolution Imaging Spectroradiometer (MODIS) imagery into four types: sugar, gravel, fish, and flowers. Different states of organization have different cloud properties including boundary layer depth, amount of precipitation, cloud fraction, and cloud radiative effect.

On February 2–3, 2020, a transition from small and shallow clouds called "sugar" to larger and deeper clouds called "flowers" occurred over the field campaign region (Figure 1a; animation in Movie S1). Backward trajectories following the airmass at 500 m altitude show that these flower clouds originated from a shallow sugar cloud layer northeast of National Oceanic and Atmospheric Administration's (NOAA) Research Vessel Ronald H. Brown (RHB). Larger flowers with cold pools were observed to the southwest, closer to Barbados. This study uses a Lagrangian LES, with the domain following a boundary-layer trajectory (red box and yellow dots in Figure 1a), to simulate this organization event. To understand the relationship between the large-scale vertical velocity and the transition of the mesoscale organization, an additional LES with modified large-scale vertical velocity is included.

The structure of this paper is as follows. Section 2 describes the simulation configurations and the observations used to initialize the simulations. Sections 3 shows the transition from sugar to flowers represented by the LES. Section 4 discusses the mechanisms that are important for the organization. Section 5 identifies the role of large-scale vertical motion on the sugar-to-flowers transition and the circulation at the mesoscale. Finally, conclusions are given in Section 6. Appendices A–D are found at the end of the manuscript (Movies S1–S3).

2. Data and Simulations

The system for atmospheric modeling (SAM) (Khairoutdinov & Randall, 2003) is employed. The large-scale meteorology and forcings of the simulations are derived from the European Center for Medium-Range Weather Forecasts (ECMWF) Reanalysis 5th Generation (ERA5) (Hersbach et al., 2020), following an airmass that passes through the location of the RHB (54.5°W and 13.9°N) at 17 UTC on February 2. The airmass trajectory was calculated by the Hybrid Single-Particle Lagrangian Integrated Trajectory (HYSPLIT) model (Rolph et al., 2017; Stein et al., 2015). With the airmass source from the RHB at 500 m altitude, the

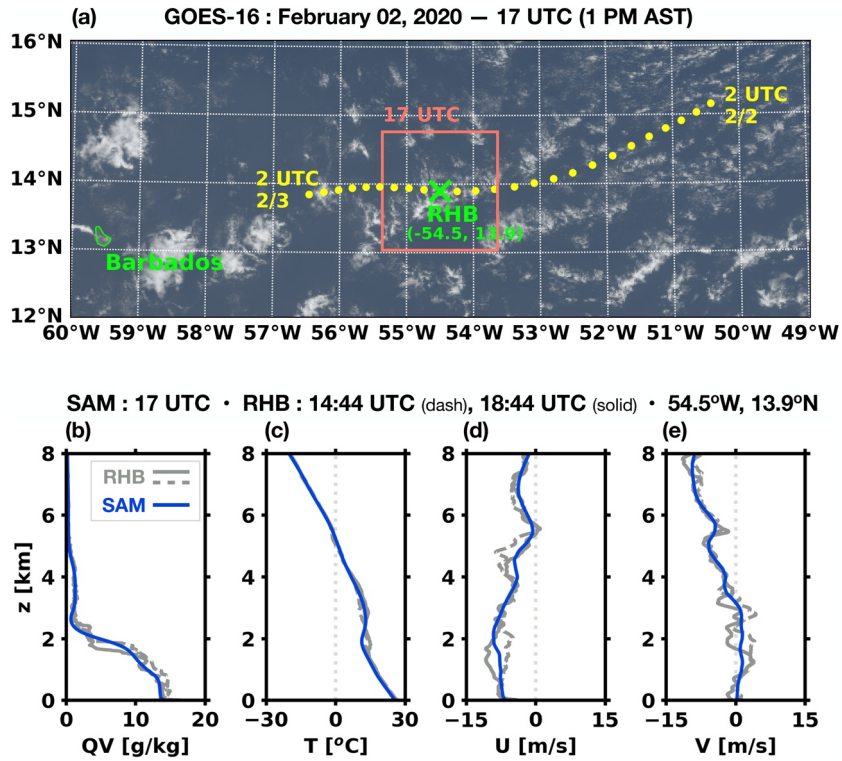

Figure 1. (a) A satellite image from the Geostationary Operational Environmental Satellite-16 (GOES-16) on February 2, 2020. The yellow dots represent hourly coordinates of the airmass-following trajectory on which the Lagrangian simulations are based. The red box indicates the simulation's 192×192 km^2 domain extent, centered on the Research Vessel Ronald H. Brown (RHB, green "×") at 17 UTC. (b)–(e) The comparisons between radiosondes from the RHB (gray) and domain-mean profiles from the System for Atmospheric Modeling (SAM) control simulation (blue) of the following variables: water vapor mixing ratio (QV), temperature (T), zonal wind (U) and meridional wind (V). The RHB radiosondes are taken at 14:44 UTC (dashed) and 18:44 UTC (solid), during which time the RHB is within SAM's domain.

trajectory was run backward to February 1 and forward to February 3. The ERA5 data, which contains 137 vertical levels, are interpolated to the latitudes and longitudes of the trajectory, making use of ERA5's full vertical resolution, especially for the vertical velocity forcings. The horizontal winds are nudged toward ERA5 with Newtonian relaxation, with a 30 min time scale. Since the trajectory moves approximately with the boundary layer, large-scale horizontal advection of the temperature and humidity is not included. Instead, to account for horizontal advection in the free troposphere, the temperature and humidity profiles of the simulation are nudged toward ERA5 with a 30 min relaxation time scale. The temperature and humidity nudging begins 100 m above the inversion, defined as the height of maximum vertical gradient of liquid water static energy in SAM (or of liquid water potential temperature in ERA5, whichever is higher). From this nudging base level, the nudging tendencies increase smoothly over a height interval of 500 m from a value of zero to a value corresponding to the nudging. The surface fluxes are calculated by SAM based on the horizontal wind speeds nudged toward ERA5, and the temperature and humidity profiles calculated by SAM in the boundary layer. Figures 1b–1e show that at the times when the trajectory is within 1° distance from the RHB, the outputs from SAM are consistent with the RHB radiosondes.

2.1. Simulations

The control simulation (CTL) is configured with 100 m horizontal grid spacing and a horizontal domain extent of 192×192 km^2. The vertical grid spacing is 50 m, increasing geometrically from 5 km to the domain top at 8 km (total of 120 levels). Above that, the atmospheric profiles from ERA5 are used up to the top of the atmosphere for the radiation calculation. The simulation uses a bulk two-moment (bin-emulating)

microphysics scheme (Feingold et al., 1998) and the Rapid Radiative Transfer Model for global climate model applications (RRTMG) (Mlawer et al., 1997) with time varying atmospheric profiles above the domain top and the diurnal cycle of solar radiation. The radiation is computed every 10 s. The model's time step is 2 s, and the duration of the simulation is 24 hr, from 2 UTC on February 2 to 2 UTC on February 3, 2020.

An additional simulation called WeakW is performed using the same model configuration as CTL, except with a modified vertical velocity (W) in the forcings. The W profiles for WeakW are 50% weaker than CTL during a period with strong upward motion, between 11 and 19 UTC. Since SAM linearly extrapolates the hourly W forcing profiles to the model's time step, W in WeakW diverges from CTL at 10 UTC, and converges again at 20 UTC (Figures 3b and 3c).

2.2. The Initialization of Aerosol

There are two types of aerosol in the simulations: sea salt and mineral dust. Sea salt is included as it is the dominant non-dust aerosol type during for particles with diameters smaller than 10 μm, based on the shipboard measurement from the RHB (Quinn et al., 2020). Mineral dust was also present in the free troposphere east of Barbados during this time. The RHB radiometer measurements, together with the surface aerosol measurements, indicated the presence of scattering and absorbing aerosol in the free troposphere (Quinn et al., 2020). Visual observation during flights of the ATOMIC field campaign confirmed the presence of such aerosol above the cloud tops. Therefore, sea salt and mineral dust are initialized at the beginning of the simulation and allowed to advect vertically by large-scale vertical velocity, and horizontally within the domain by trajectory-relative horizontal winds throughout the simulation. The sea-salt particles interact with the cloud microphysics scheme, while the mineral dust is coupled with the radiation scheme. See Appendix A for details on the initialization of the aerosol species.

3. Transition of Shallow Cumuli: From Sugar to Flowers

Simulation CTL is able to reproduce the transition from sugar to flowers on February 2–3, 2020. Figures 2a–2e show 192×192 km^2 snapshots from GOES-16 along the trajectory on which the simulation is based. Figures 2f–2j and Movie S2 show the cloud state evolution from CTL. A comparison between the snapshots from GOES-16 and CTL shows that SAM reproduces the nature of the transition well, although there are some disagreements between the satellite images and the simulation. In particular, the satellite imagery shows greater variability in cloud structure over the same area compared to the simulation domain.

The sugar-to-flowers transition in CTL occurs between 8 and 18 UTC, consistent with GOES-16 except the satellite shows larger cloud clusters forming along a line toward the south. During this time, the sugar cloud fields in CTL develop into contiguous aggregates and expand laterally to mature into flowers. As the initial sugar clouds organize, some interspersed cumulus clouds are suppressed, while the ones that have aggregated persist and grow. After 24 UTC the simulated cloud clusters expand and catch up with those captured by GOES-16. The aggregated flowers in CTL produce precipitation, which partially evaporates before reaching the surface, resulting in cold downdrafts that produce cold pools adjacent to the flowers.

Potential reasons for the discrepancy between SAM and GOES-16 could result from errors in ERA5 profiles and sea surface temperature, and the model physics. Furthermore, unlike regional models, SAM (and other LES) represent conditions at one particular location rather than the entire region of the satellite images. SAM operates with spatially invariant top, bottom, and lateral boundary conditions, the latter of which are periodic. However, in reality the area covered by the simulation domain experiences spatial variability in boundary conditions, and lateral boundary conditions are not periodic. Hence, we expect variability in the simulations to be smaller than compared to reality over the simulated area, with the simulation capturing the real cloud state only within a limited sub-region of the area seen in the satellite imagery. Nonetheless, the mean states from SAM are still consistent with the observations, as shown in Figures 1b–1e. Because the simulation still faithfully captures the general nature of this transition as seen in the satellite, the analysis is representative of what happens in reality.

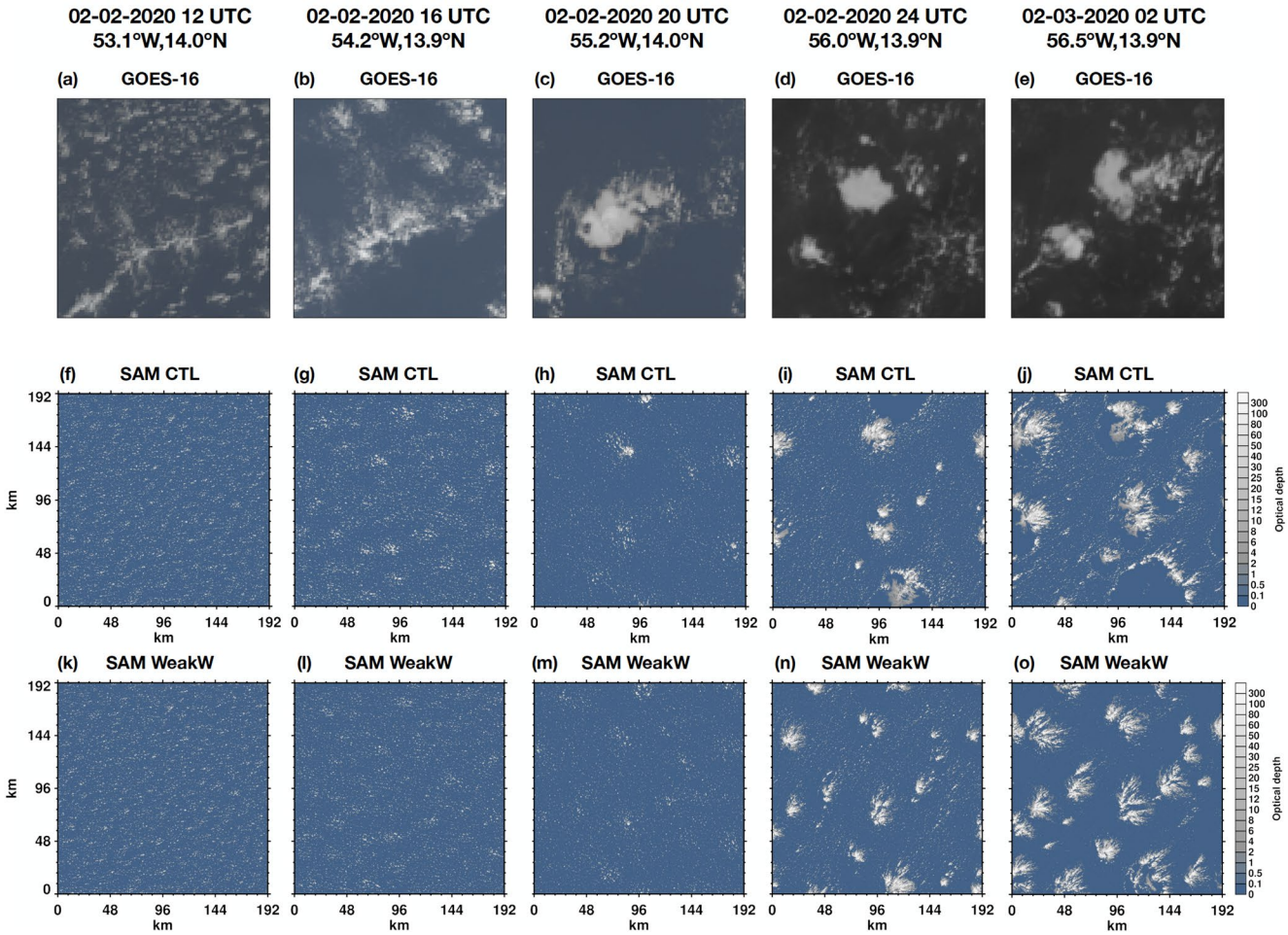

Figure 2. Comparisons of GOES-16 and System for Atmospheric Modeling (SAM) simulations over a 192 ×192 km^2 domain at 12, 16, 20, and 24 UTC on February 2, and 2 UTC on February 3, 2020. (a–e) Satellite images from GOES-16, centered on the trajectory presented in Figure 1. (f–j) Snapshots of total (cloud + rain) optical depth from SAM control simulation (CTL). (k–o) As in Panels (f–j) but for the weaker vertical velocity simulation (WeakW). A high-resolution version of this figure is found in Figure S1.

3.1. Multiscale Partitioning

Although the simulations are run at 100 m grid spacing, it is helpful to coarse-grain the outputs into larger tiles. This approach partitions the results into contributions from the large-scale, mesoscale, and cumulus-scale processes (BB2017). Coarse-graining filters out the details at the smaller scales that may be associated with shallow convection but are not relevant to the organization. Similar to the approach taken by Honnert et al. (2011), the variance of total water path is computed at different scales (Appendix B). Total water path (TWP) is defined as the sum of vertically integrated water vapor, cloud, and rain (Figure C1). A tile size of 16 × 16 km^2 is chosen for this study as it represents the horizontal variability of moist patches associated with flower shallow cumuli in the simulations.

The partitioning of total water mixing ratio (q_t) is given by:

$$q_t = \overline{q_t} + q_t'' + q_t'''. \quad (1)$$

The overline is the domain-mean, the double prime is the perturbation coarse-grained to 16 × 16 km^2 tiles, representing variability associated with the mesoscale (≥16 km). The triple prime represents variability associated with cumulus-scale processes (<16 km). The partitioning is detailed in Appendix D1.

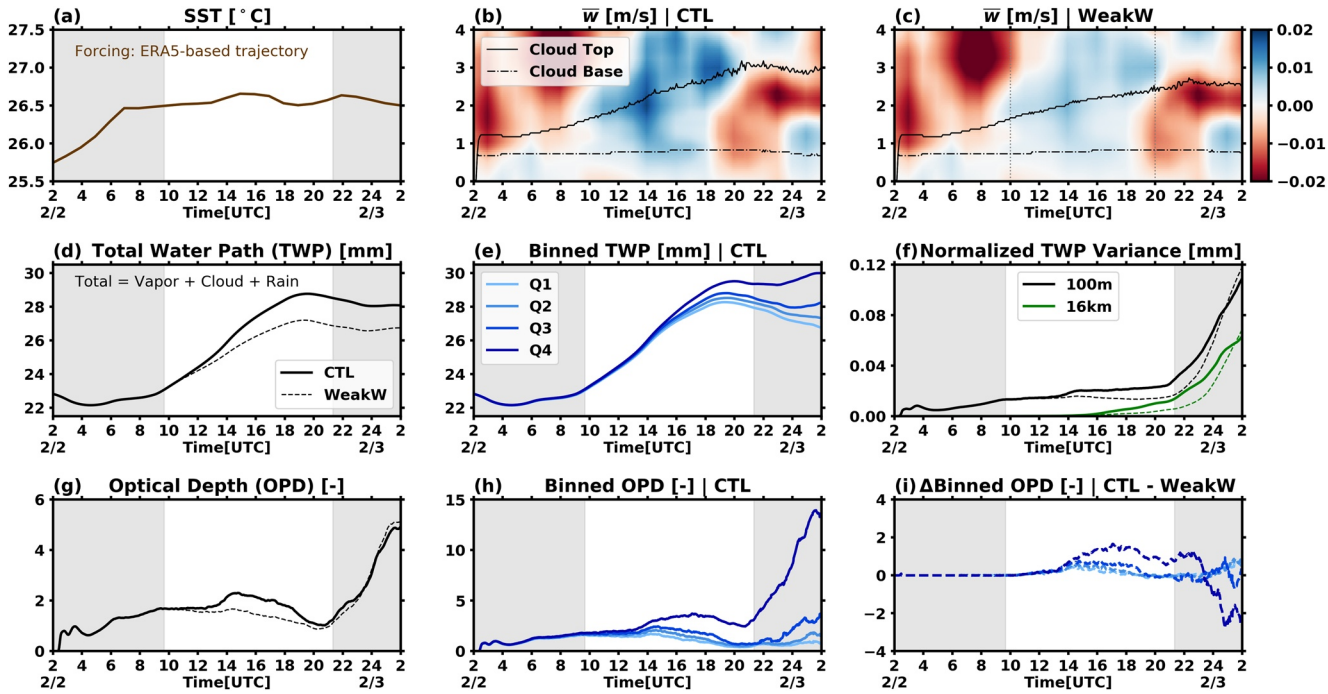

Figure 3. Time series of: (a) Domain-mean sea surface temperature; (b) Domain-mean vertical velocity, and cloud top and base heights, from CTL; (c) As in panel (b) but for WeakW; (d) Domain-mean total water path (TWP) of both CTL (solid) and WeakW (dash); (e) TWP sorted into quartiles from CTL; (f) Variances of TWP computed at the full resolution (black) and the 16 km coarse-grained resolution (green), from both CTL (solid) and WeakW (dash); (g) Domain-mean optical depth (OPD) from both simulations; (h) OPD from CTL binned by TWP into quartiles; (i) The change in OPD, binned by TWP, between CTL and WeakW. Gray shading is applied between the daylight hours of 5:48 a.m. and 17:23 p.m. (local time), when the top-of-atmosphere incoming shortwave radiation exceeds zero in System for Atmospheric Modeling (SAM).

The coarse-grained outputs are sorted by TWP and binned into quartiles. Quartile 1 (Q1) represents the driest and cloud-free areas while Quartile 4 (Q4) represents the moistest and cloudiest areas of the simulation. The 16×16 km^2 tiles in each quartile are not necessarily adjacent to one another.

3.2. Shallow Convection Organization

Figure 3 shows the time series of the simulations. The thick solid lines represent the results from CTL. Sea surface temperature (SST) increases as the trajectory moves southwestward, and remains constant as the trajectory moves westward. The deepening of the cloud layer in CTL occurs after 6 UTC and becomes more obvious after 10 UTC, when the domain-mean vertical velocity ($\overline{w}$) shifts from negative to positive, helping the cloud layer to deepen (Figure 3b). After 20 UTC, the cloud depth remains constant as the boundary layer encounters large-scale subsidence.

The domain-mean TWP increases as the cloud layer deepens during the transition (Figures 3d and C1). As the organization strengthens after 12 UTC, the TWP distribution becomes more asymmetrical; the moist areas become moister while the dry areas become drier (Figure 3e). The variance of TWP normalized by the mean can be used as a proxy for the organization strength (Figure 3f). The full 100-m resolution variance (black) increases first at 12 UTC, followed by the coarse-grained variance (green) which increases around 16 UTC; both of them increase rapidly after 22 UTC. This indicates that the organized moist patches first strengthen gradually, and later the organization accelerates. During the transition, the total optical depth (OPD) increases, except for a dip around 20 UTC (Figures 3g and 3h), when the small isolated sugar clouds disappear while the larger cloud clusters have yet to aggregate and grow (Figure 2h). After 20 UTC, the OPD also increases rapidly as the organization strengthens further. The first cold pool is observed at 22 UTC (Movie S2). Because the shallow cumuli in CTL do not precipitate until 20 UTC (Figure C1c), approximately 4 hr after the mesoscale organization starts to take place, precipitation is not essential for organization in

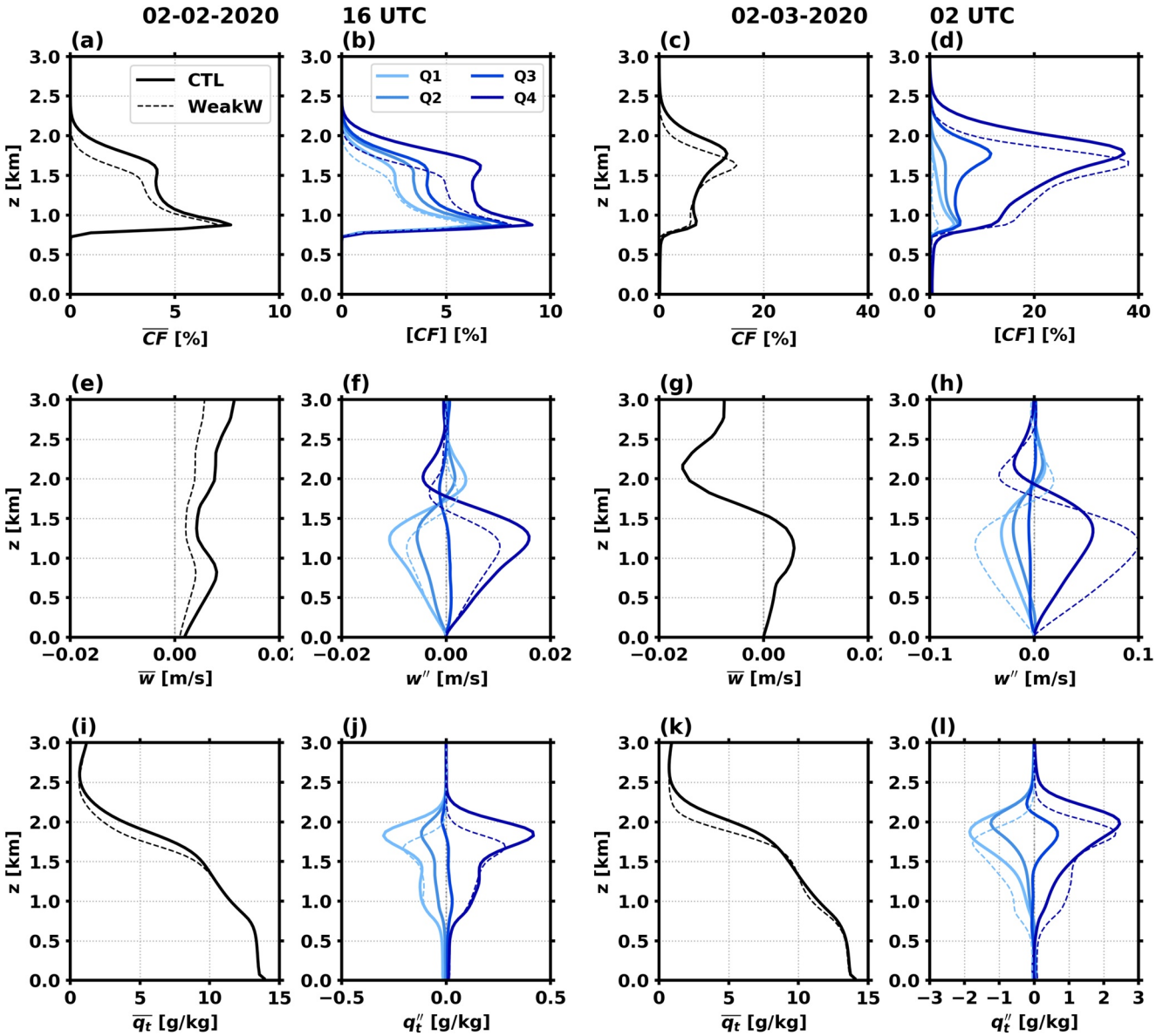

Figure 4. Vertical profiles of various variables at 16 UTC on February 2 (two left columns) and 2 UTC on February 3 (two right columns) of both CTL (solid) and WeakW (dash): (a and c) Domain-mean cloud fraction ($\overline{CF}$); (b and d) Cloud fraction binned by total water path (TWP) quartiles (CF); (e and g) Vertical velocity ($\overline{w}$); (f and h) Mesoscale perturbations of vertical velocity binned by TWP quartiles (w''); (i and k) Domain-mean total water mixing ratio ($\overline{q_t}$); and (j and l) Mesoscale perturbations of total water (q_t''), binned by TWP quartiles. For the binned profiles, only Q1 and Q4 from WeakW are shown.

the considered case. This finding is consistent with BB2017, but different from Seifert and Heus (2013) who found that cold pool formation is a dominant mechanism leading to cloud cluster formation.

Figure 4 shows the vertical profiles at two different times, during and after the sugar-to-flowers transition. At 16 UTC on February 2, the domain-mean cloud fraction ($\overline{CF}$) and cloud fraction binned by TWP quartiles (CF) are bottom-heavy, with slightly enhanced cloudiness near the cloud top in Q4. The enhanced cloudiness near cloud top indicates that the clouds begin to transition from the sugar state to the flower state. At 2 UTC on February 3, the profiles become top-heavy, showing stratiform cloudiness, which is a distinct feature of the flower clouds (Bony et al., 2020; Rasp et al., 2020; Stevens et al., 2020). The stratiform cloudiness near the shallow cumulus cloud top is associated with pronounced longwave radiative cooling (Figures C2a and C2c), consistent with previous studies (Vogel et al., 2020).

At both times, regardless of the cloud states and the large-scale vertical velocity ($\overline{w}$), the binned mesoscale vertical velocity perturbations (w'') are positive in the cloud and subcloud layers and negative in the inversion layer of the moistest quartile (Q4). In the drier quartiles (Q1–Q2), the signs of w'' are opposite. The moist quartiles also have positive mesoscale total water perturbations (q_t''). These mesoscale perturbation profiles from Simulation CTL, which was driven with large scale meteorology from the ERA5 reanalysis, exhibit similar behaviors to those simulations with the weak temperature gradient approximation in BB2017, except with larger magnitudes of perturbations at 2 UTC in CTL.

Figures C2b and C2d further show that the longwave radiative heating perturbations (R''_{LW}) are negative (more cooling) in the inversion layer of the moistest quartile where q_t'' is also positive and large, and positive (more heating) in the cloud and subcloud layer. This suggests that longwave radiation generates relatively more buoyant air in the cloud plume and less buoyant air in the inversion aloft, contributing to the mesoscale circulation between the moist and dry regions. During the daytime, the longwave radiation is almost balanced by the shortwave radiation (Figures C2e and C2f), resulting in a negligible radiative contribution in the boundary layer, similar to BB2017. In the moist regions, there is also more latent heating in the subcloud and cloud layers due to more condensation, and more evaporative cooling in the inversion layer (Figures C2j and C2l), which also contributes to w'', consistent with BB2017.

Mass continuity requires that in the moist and cloudy regions, where w'' is positive (negative) in the subcloud (inversion) layer, there is a local convergence (divergence) below (aloft) (see also BB2017). The profiles at both times have the same signs, but larger magnitudes at 2 UTC on February 3. This is because the cloud clusters are larger at the later time; therefore, coarse-graining does not wash out the variability associated with larger cloud clusters. Although cold pools are observed at the later time, at this stage of cold pool development, there is no significant difference in the dynamics (w'') compared to the stage prior to their formation. The same underlying mechanism associated with the mesoscale circulation still dominates. The following section will show that this local circulation is key to redistributing the total water, leading to mesoscale organization.

4. The Mechanism of Transition

This section analyzes the budget of mesoscale total water perturbations q_t'' in the four TWP quartiles to determine a mechanism responsible for the transition. In each TWP quartile, the mesoscale tiles are not necessarily adjacent to one another and they can change location in time based on the mesoscale TWP. Based on Equation 12 of BB2017 and the derivation in Appendix D, the budget of q_t'' at each level can be written as:

$$\frac{\partial q_t''}{\partial t} = A + B + C + S_q''. \tag{2}$$

Each term on the right hand side of Equation 2 is described as follows: The first term is the advection of mesoscale variability due to trajectory-relative large-scale wind ($\overline{\boldsymbol{v}}$) and mesoscale perturbations of the wind velocity ($\boldsymbol{v}''$):

$$A = -(\overline{\boldsymbol{v}} + \boldsymbol{v}'') \cdot \nabla q_t''. \tag{3}$$

Let $[\ \ ]$ denote coarse-graining of the cumulus-scale field inside the brackets to a mesoscale region of 16×16 km^2, and let ρ denote the reference density profile. The second term represents the vertical and horizontal gradients of the cumulus-scale q_t flux coarse-grained to 16×16 km^2:

$$B = B_v + B_h = -\frac{1}{\rho}\frac{\partial}{\partial z}[\rho w''' q_t'''] - \nabla_h \cdot [\boldsymbol{v}''' q_t'''] . \tag{4}$$

Equation 4 was derived with the anelastic approximation used in SAM. The third term is the mesoscale vertical advection of large-scale q_t:

$$C = -w'' \frac{\partial \overline{q_t}}{\partial z}. \tag{5}$$

Finally, the fourth term is the source term of q_t'', which represents the mesoscale perturbations of the precipitation mass flux (F_p) divergence:

$$S_q'' = \left(-\frac{1}{\rho}\frac{\partial F_p}{\partial z} \right)'' . \tag{6}$$

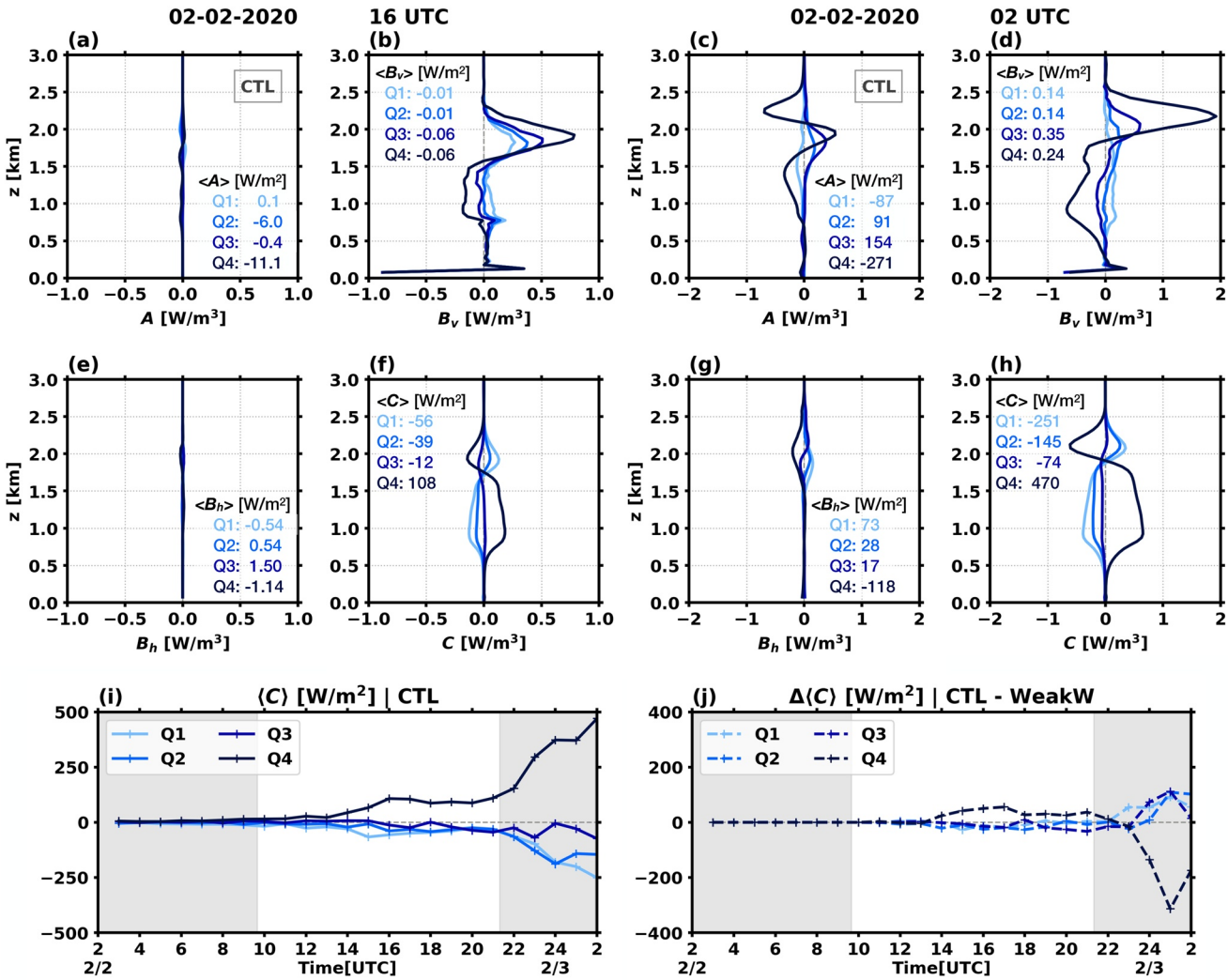

Figure 5. Vertical profiles of: (a and c) Large-scale and mesoscale advection of q_t'' (A); (b and d) Vertical gradient of the cumulus-scale vertical q_t flux (B_v); (e and g) Horizontal gradient of the cumulus-scale horizontal q_t flux (B_h); and (f and h) Mesoscale vertical advection of the large-scale q_t (C), at 16 UTC on February 2 (two left columns) and 2 UTC on February 3 (two right columns) from CTL, all coarse-grained to 16×16 km^2 tiles and binned by TWP. The vertically integrated values between 0 and 3 km are also shown, denoted by $\langle \quad \rangle$. (i) Hourly time series of $\langle C \rangle$ binned by TWP quartiles from CTL. (j) The change in $\langle C \rangle$ time series between CTL and WeakW.

Figures 5a–5h show vertical profiles of A, B_v, B_h, and C binned by TWP quartiles from CTL at 16 UTC on February 2 (two left columns) and 2 UTC on February 3 (two right columns). In each panel, the vertically integrated value of the respective quantity between 0 and 3 km (denoted by $\langle \quad \rangle$) is also shown. (The S_q'' profiles and their vertically integrated values are much smaller and hence negligible even at 2 UTC on February 3, when the clouds precipitate, as shown in Figure C3a). A positive quantity means the respective term is responsible for moistening the region, a source term for q_t''.

According to BB2017, A is small and tends to dry out the boundary layer in Q4. Although this is true at 16 UTC on February 2 (Figure 5a), A has a non-negligible magnitude in the cloud layer at 2 UTC on February 3 (Figure 5c). Nonetheless, $\langle A \rangle$ still dries out Q4, and A is not a major term in the q_t'' budget.

Although B_v is large at both times, $\langle B_v \rangle$ is negligible in all quartiles. This is expected because the vertical cumulus-scale flux transfers total water vertically from the cloud layer to the inversion layer but not horizontally. When coarse-grained within 16×16 km^2 regions, B_h is small and negligible at 16 UTC on February 2, but $\langle B_h \rangle$ is non-negligible at 2 UTC on February 3 and contributes to drying in Q4, albeit secondary to $\langle A \rangle$.

At both times, the magnitude of C is larger than that of A and B_h, and $\langle C \rangle$ is the only term that moistens the boundary layer in Q4, in which flower clouds aggregate. Because $\frac{\partial \overline{q_t}}{\partial z}$ is always negative (Figures 4i and 4k), the sign of C always follows the sign of w''. Due to mass continuity, a positive C in the cloud layer of Q4 is associated with horizontal total water convergence below the cloud plumes, and divergence in the inversion. A positive $\langle C \rangle$ indicates a net total water convergence in the lower troposphere of the moistest quartile.

To demonstrate that $\langle C \rangle$ drives moistening in Q4 and drying in Q1–Q3, Figure 5i shows the hourly time series of $\langle C \rangle$ binned by TWP quartiles from CTL. This provides the evidence that the net convergence and divergence of total water due to mesoscale circulation renders the moist and cloudy patches moister, and the dry and cloud-free patches drier.

5. The Role of Large-Scale Upward Motion

To examine the role of large-scale vertical velocity for the sugar-to-flower transition, an additional simulation is performed and analyzed. Simulation WeakW has a 50% weaker $\overline{w}$ during the period of strong upward motion, that is, between 10 and 20 UTC which is referred to as the intermediate state of the sugar-to-flower transition (Figure 3c). The period after that is referred to as the final organization state. Figures 2k–2o and Movie S3 show the cloud field evolution in WeakW. Similar to CTL, the sugar clouds in WeakW aggregate into flower clusters and expand laterally as the cloud layer deepens. The flower clouds in WeakW are initially smaller and barely precipitate, whereas in CTL the clouds precipitate sooner and more strongly (Figure C1c), so more and larger cold pools form in the final organization state of CTL. In WeakW, more but smaller flowers form at the end, and also there are fewer smaller interspersed clouds between the flower clusters.

Because of the weaker upward motion during the intermediate state of the transition, WeakW produces a shallower boundary layer that contains a smaller amount of vertically integrated water vapor, and has lower TWP than in CTL. The boundary layer in WeakW is also less decoupled, as measured by the relative decoupling index (Figure C4) (Kazil et al., 2017). During the intermediate state, Simulation CTL exhibits a more rapid transition from the sugar to the flower cloud state than WeakW. It has greater normalized TWP variances and total optical depth, especially in Q4 where flowers aggregate (Figures 3f and 3i). Although mesoscale organization forms more rapidly in CTL during this state, the same mechanisms take place in both simulations. Moist areas become moister and dry areas become drier. Figures 4f and 4j show that with stronger upward motion, the w'' and q_t'' profiles of CTL during the transition period have the same structure as those in WeakW, except with larger magnitudes. In other words, the stronger upward motion deepens the boundary layer and enhances the mesoscale circulation (w'') which assists the aggregation of total water in the mesoscale, thus accelerating the organization.

The final organization state in WeakW catches up with and becomes stronger than CTL, as measured by higher normalized TWP variances (Figure 3f). After 23 UTC, the TWP variances (with and without normalization) in WeakW increase and later become higher than in CTL, but the domain-mean TWP in CTL remains higher (Figure 3d). This is because the dominant term in TWP is water vapor; it is concentrated within the boundary layer, which is deeper in CTL. As the organization in WeakW catches up, w'' becomes stronger in WeakW than in CTL (Figure 4h) and the stronger mesoscale circulation helps redistribute the total water such that the moist areas become moister quickly. This is consistent with the change in $\langle C \rangle$, which is greater in Q4 of CTL compared to WeakW between 10 UTC and 23 UTC (Figure 5j), and smaller thereafter.

Figure 6 shows the spectra of buoyant turbulence kinetic energy (TKE) production in the cloud layer, or TKE_b(IC), and of boundary-layer total water variance, or q_t (BL), derived from CTL, as well as the ratios of the spectra in CTL and WeakW. Circulation on the mesoscale and aggregation of moisture emerge in the form of peaks between 9.6 and 16 km that are clearly discernible by 10 UTC (Figures 6a and 6d) and continue to grow upscale as the clouds transition to the flower state (Figures 6b and 6e). Up to 10 UTC, CTL and WeakW have the same $\overline{w}$, hence the spectra are identical and the ratios of TKE_b (IC) and q_t (BL) spectra are 1 (Figures 6c and 6f).

In the following hours, the ratio of TKE_b (IC) spectra increases (Figure 6c), suggesting that the stronger large-scale upward motion renders TKE production stronger in CTL compared to WeakW. The subcloud

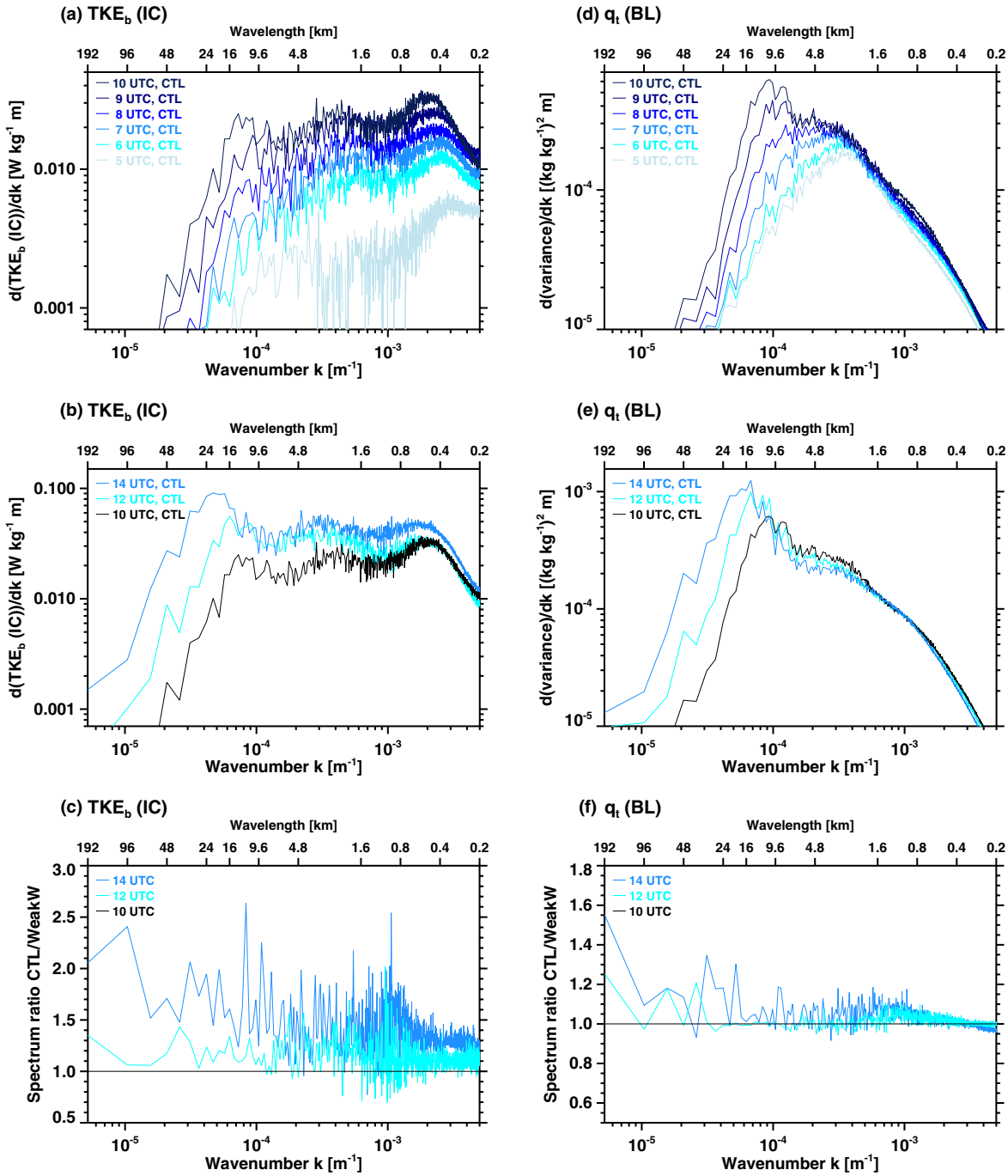

Figure 6. (a–b) Spectra of buoyant turbulence kinetic energy production in the cloud layer, or TKE$_b$(IC), expressed in units of W kg^{-1} of boundary-layer mass, plotted hourly from 5 to 10 UTC and bi-hourly from 10 to 14 UTC, respectively. (c) Ratio of the TKE$_b$ (IC) spectra in CTL and WeakW plotted at 10, 12, and 14 UTC. (d–f) As in panels (a–c) but for total water mixing ratio in the boundary layer, or q$_t$ (BL).

layer, on the other hand, consumes TKE production at specific mesoscale wavelengths (see Appendix C and Figure C5). This indicates that the mesoscale circulation that emerges in the sugar-to-flower transition is predominantly driven by TKE production in the cloud layer. Finally, the ratio in the q$_t$ (BL) spectra remains noisy at 12 UTC and increases at 14 UTC (Figure 6f), albeit at a smaller magnitude than the TKE$_b$ (IC) spectra. This is evidence that stronger large-scale upward vertical motion strengthens both the mesoscale TKE production and the moisture aggregation, the former more than the latter.

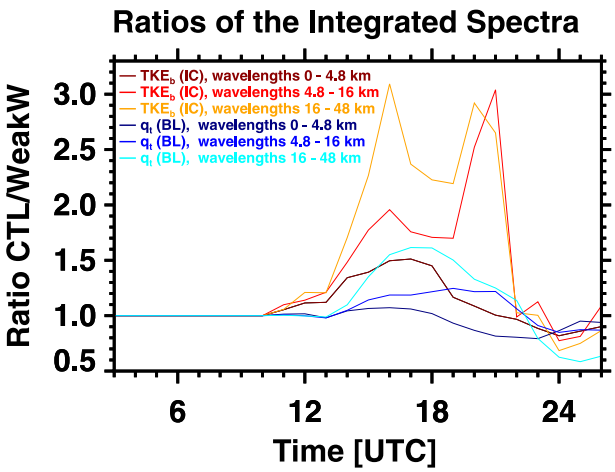

Figure 7. Time series of the ratio of integrated TKE_b (IC) spectra (warm colors) and the ratio of integrated q_t (BL) spectra (cool colors). The ratio is between simulations CTL and WeakW. The spectra are integrated at three different wavelength bands: 0–4.8 km (small-scale), 4.8–16 km (meso-γ-scale), and 16–48 km (meso-β-scale).

Figure 7 shows the ratio of integrated TKE_b (IC) and q_t (BL) spectra in CTL and WeakW. The spectra are integrated at three different wavelength bands, 0–4.8, 4.8–16, and 16–48 km. From the moment the two simulations diverge, that is, 10 UTC, the ratio of the TKE production at the mesoscale (4.8–16 km and 16–48 km) exceeds the ratio of the TKE production at the smaller scale (0–4.8 km). This disproportionate strengthening of cloud-level mesoscale TKE production relative to other scales, due to the more positive $\bar{w}$ in CTL compared to WeakW, increases and persists over the period during which $\bar{w}$ differs between the simulations. Additionally, the increase in the ratio of the TKE production leads a corresponding increase in the ratio of the QT variance by approximately 3 hr, which indicates a causal relationship between the TKE production and the redistribution of the moisture. Therefore, it is the strengthening of cloud-level mesoscale TKE production in CTL relative to WeakW that strengthens aggregation of moisture on the mesoscale and accelerates the sugar-to-flower transition in response to a more positive $\bar{w}$.

6. Conclusions

The ATOMIC and EUREC^{4}A field campaign took place in the Atlantic Ocean east of Barbados in January–February 2020, with a goal of better understanding the relationship between shallow cumuli and large-scale meteorological and oceanic conditions. On February 2–3, a transition of trade cumulus organization from sugar to flowers were observed. This study shows that a Lagrangian LES following a boundary-layer airmass trajectory can reproduce the transition. During the sugar-to-flowers transition, the clouds become organized, and the cloud layer deepens and moistens.

Although the large-scale vertical motion helps deepen the cloud layer, the mesoscale wind drives the sugar-to-flowers transition. The mesoscale circulation, driven by local ascending (descending) air inside (above) the shallow cumulus plumes, leads to a net moisture convergence in the moist patches, in which the clouds aggregate. This renders the moist patches moister and dry patches drier.

It is shown that large-scale vertical velocity regulates the sugar-to-flower transition by modulating cloud-layer buoyant TKE production at the mesoscale, and the mesoscale circulation by which moisture aggregates. In the considered case, stronger large-scale upward motion accelerates the sugar-to-flower transition by strengthening cloud-layer mesoscale TKE production.

Given the broad interest in the vertical structure of subsidence engendered by ATOMIC and EUREC^{4}A, a follow-on study examining how the structure of the large-scale vertical velocity impacts the mesoscale organization is warranted. Because of the presence of mineral dust, a follow-on study examining the sensitivity of the shallow cumulus organization to mineral dust will be conducted. Precipitation and cold pools may also affect the rate of mesoscale organization and the cloud cluster sizes; hence, a future study will also explore these relationships.

Appendix A: The Initialization of Sea Salt and Mineral Dust

Sea salt and mineral dust are initialized at the beginning of both the CTL and WeakW simulations (see Section 2.2 and Figure A1). The details on the initialization are as follows.

Appendix A1. Sea-Salt Particles

The sea-salt particles in the boundary layer are initialized based on in-situ aerosol data measured from the RHB averaged between 0 and 4 UTC on February 2. The aerosol size distribution is bimodal and fitted with lognormal functions (Figure A2). The first peak has a geometric mean diameter (D_g) and geometric

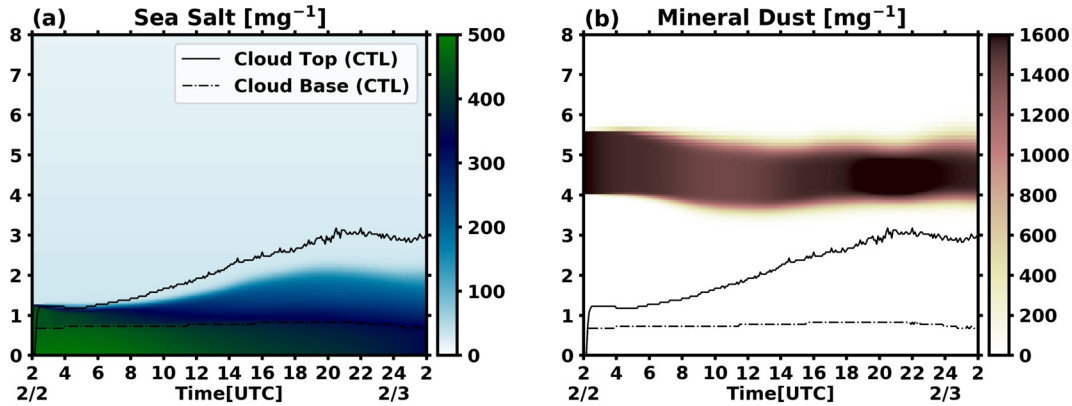

Figure A1. Time series of the domain-mean (a) Sea salt and (b) Mineral dust concentration from control simulation. In both panels, the solid and dash-dot lines indicate the cloud top and cloud-base heights of the simulation.

standard deviation (σ_g) of 0.128 μm and 1.71, respectively, and the initial concentration (N) is 400 mg^{-1}. The second peak's D_g and σ_g are 0.961 μm and 1.73, respectively, and N is 13 mg^{-1}. The sea-salt particles in the free troposphere have initial N of 32 mg^{-1}, consistent with the EUREC^{4}A measurements from the Ultra-High-Sensitivity Aerosol Spectrometer (UHSAS) and the Cloud Droplet Probe (CDP-2) on the French ATR-42 research aircraft (personal communication with Pierre Coutris, September 30, 2020). The sea salt is coupled with the cloud microphysics scheme.

Appendix A2. Mineral Dust

Mineral dust was present in an elevated layer east of Barbados between January 31 and February 3. Therefore, a mineral dust layer is placed in the simulation between 4 and 5.5 km, colocated with an elevated moist layer, based on a previous study, which showed that the long-ranged transported Saharan air layer carries mineral dust and moisture from Africa to the Caribbean (Gutleben et al., 2019). The initial mineral dust concentration inside the layer is 1,600 mg^{-1}. Dust optical properties are calculated based on the assumed size distribution and refractive indices in d'Almeida et al. (1991). The single scattering albedo is approximately 0.85. As a result, the aerosol optical depth of the mineral dust is approximately 0.35, consistent with the MODIS observation during the period of interest. The mineral dust is coupled with the radiation scheme, but not with the cloud microphysics, as the dust remains in the free troposphere in this simulation.

To confirm that the mineral dust configuration described above is consistent with the observation, two additional Eulerian simulations are performed. Figure A3 shows that the clear-sky surface radiations in SAM are more consistent with the in-situ measurements when the mineral dust is included. Since the RHB was stationary between February 1 and 2, during which there is a cloud-free period, the additional simulations' domain is fixed at the RHB location. The forcings are driven with ERA5, similar to the Lagrangian simulations presented in the main manuscript, except the large-scale horizontal advection tendency of the temperature and humidity is included. These additional simulations are configured with 50 m horizontal grid spacing and a horizontal domain extent of 40×40 km^2. The vertical grid spacing, domain top height, and cloud microphysics and radiation schemes of these Eulerian simulations are the same as those of the Lagrangian simulations. During the cloud-free period, the implemented mineral dust layer increases the surface downward shortwave radiation by approximately 70 W/m^2, making it more consistent with the observation from the RHB. The contribution of the mineral-dust layer on the surface longwave radiation is small, albeit in the right direction.

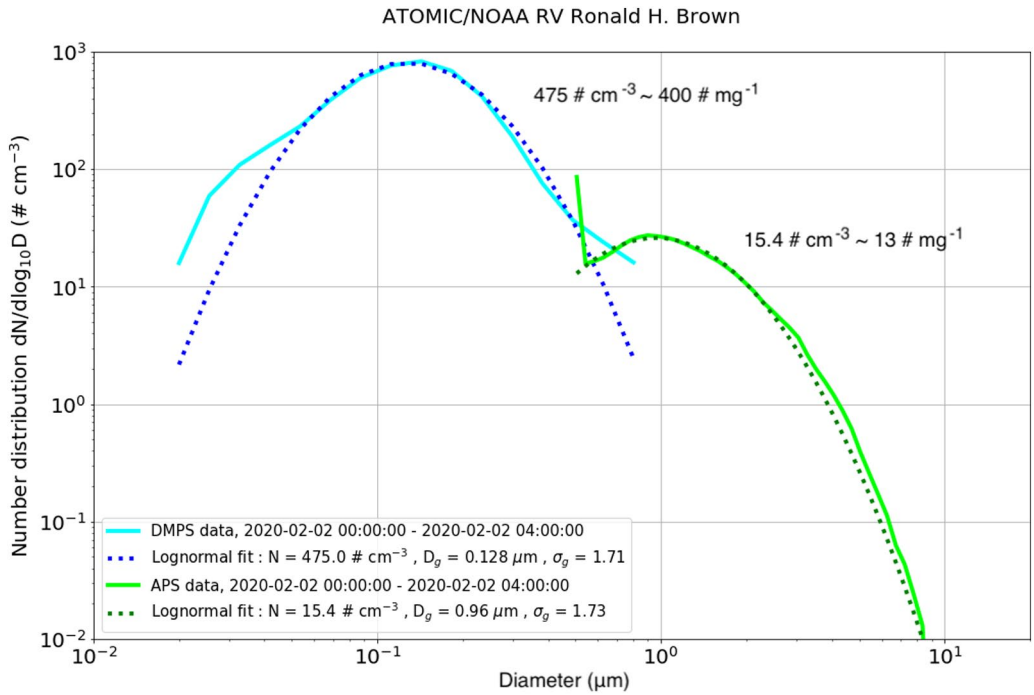

Figure A2. Aerosol size distribution (solid lines) measured from the Research Vessel Ronald H. Brown, averaged between 0 and 4 UTC on February 2, 2020, used to initialize sea-salt aerosol in the simulations. The aerosol size distribution is bimodal and fitted with lognormal functions (dotted lines).

Appendix B: Determining the Tile Size for Coarse-Graining

The ratio of total water path variance is used to determine the tile size for coarse-graining. The ratio is between TWP coarse-grained to different tile sizes, or $\mathrm{Var(TWP)}_{\mathrm{Tile}}$, and TWP at the full 100 m resolution, or $\mathrm{Var(TWP)}_{100\ \mathrm{m}}$, and is referred to as the "TWP variance ratio" for short. (See Honnert et al., 2011 for examples of this approach being applied to other variables). Figure B1 shows the TWP variance ratio from 4 UTC on February 2, 2020 to 2 UTC on February 3, 2020, plotted every 2 hr from CTL. The tile sizes are multiples of the horizontal grid spacing, from 200 m to 64 km. The TWP variance ratio is 1 if the tile size is 100 m (the horizontal grid spacing), and reduces to smaller values as the tile sizes become larger. When the TWP variance ratio is below the *e*-folding value (horizontal gray line), the tile size is too coarse to represent the variability of TWP within the domain on the scale represented by the tile. Since the mesoscale organization strengthens rapidly after 20 UTC, as measured by the normalized TWP variance (Figure 3f), we look for the tile sizes that can still represent the variability of TWP within the domain after that time. The TWP variance ratio from CTL is above the *e*-folding value between 20 UTC on February 2 and 2 UTC on February 3 for the tile size of 16 km. Therefore, we pick 16 km as the tile size for coarse-graining in CTL.

Appendix C: Additional Figures

This section provides additional figures for the discussion in Sections 3–5 of the main manuscript.

Figure C1 shows the time series of the vertically integrated water vapor (also known as precipitable water or PW), cloud water path (CWP), and rain water path (RWP). The time series are from simulations CTL and WeakW. The sum of these quantities equals the total water path (Figure 3d).

Figure C2 shows the vertical profiles from simulation CTL: (top) longwave radiative heating rate, (center) shortwave radiative heating rate, and (bottom) latent heating rate associated with net evaporation and condensation. See Section 3.2 and figure caption for details.

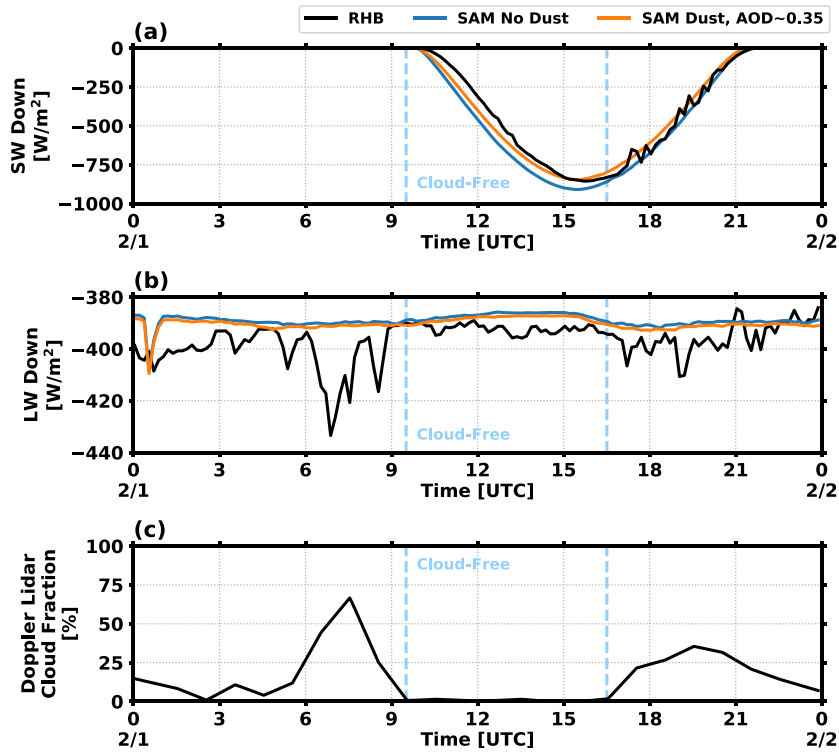

Figure A3. (a) A comparison of the downward shortwave radiation from the Research Vessel Ronald H. Brown (RHB) in-situ measurement (black) and the Eulerian simulations with mineral dust (orange) and without mineral dust (blue). (b) As in panel (a) but for the downward longwave radiation. (c) Time series of the cloud fraction measured by the Doppler lidar at the RHB.

Figure C3 shows the vertical profiles from simulation CTL of the mesoscale perturbations of the precipitation mass flux divergence at 2 UTC on February 3, and the central difference of the mesoscale total water mixing ratio perturbations about 2 UTC. Since the 3D outputs are saved every 15 min, Δt = 30min and $\langle \frac{\Delta q_t''}{\Delta t}|_{30min} \rangle$ does not necessarily equal the sum of the right hand side of Equation 2 in the main manuscript because of the large time interval. But the approximation

$$\langle \frac{\Delta q_t''}{\Delta t}|_{30min} \rangle \approx \langle A \rangle + \langle B_v \rangle + \langle B_h \rangle + \langle C \rangle + \langle S_q'' \rangle$$

still holds, and the moister quartiles get moister and the drier quartiles get drier.

Figure C4 shows the time series of the relative decoupling index (Kazil et al., 2017). It is defined as:

$$(\overline{z_{CB}} - \overline{z_{LCL}})/\overline{z_{LCL}},$$

where $\overline{z_{BC}}$ is the domain-mean cloud base height and $\overline{z_{LCL}}$ is the domain mean lifting condensation level. It is calculated based on the absolute decoupling index $\overline{z_{CB}} - \overline{z_{LCL}}$ introduced by Jones et al. (2011), normalized by $\overline{z_{LCL}}$. A higher decoupled index means the boundary layer is more decoupled.

Figure C5 shows the spectra of buoyant TKE production in the subcloud layer, or TKE_b (SC). The spectra are expressed in the unit of W kg^{-1} of boundary layer mass, enabling a comparison of the spectra in the subcloud layer with the cloud layer (Figures 6a and 6b) not only in terms of shape, but also magnitude. After 10 UTC, the TKE_b (SC) spectra decrease with time and is negative at the mesoscale (approximately 9.6–24 km

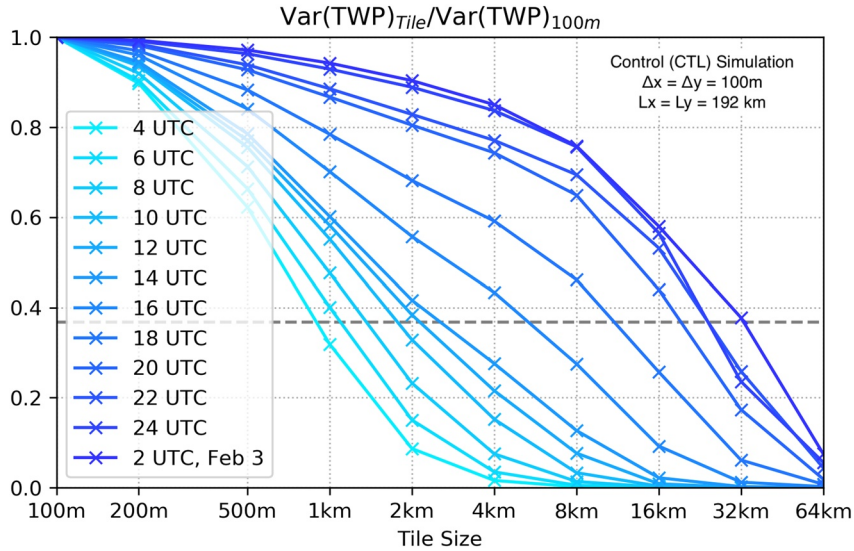

Figure B1. The total water path (TWP) variance ratio, or the ratio of the variance of total water path coarse-grained to different tile sizes to the variance of 100-m resolution total water path, or $\mathrm{Var(TWP)_{Tile}/Var(TWP)_{100\,m}}$, computed at different tile sizes from 200 m to 64 km for control simulation. The horizontal gray dash line indicates the e-folding value. See text in Section 2 above for details.

wavelength). The negative spectra do not appear on the logarithmic axis. This indicates that the subcloud layer consumes TKE at specific mesoscale wavelengths. It is the TKE production in the cloud layer that drives the mesoscale circulation, which emerges in the sugar-to-flower transition.

Appendix D: Mesoscale Tracer Budget Derivation

This section explains the derivation of the budget of a tracer on a (mesoscale) region in detail. The derivation in Appendix D3 makes no assumptions simplifying the Navier-Stokes equations. The anelastic approximation and a scale-separation approximation are applied in Appendix D4 to obtain the budget of a tracer on a (mesoscale) region derived by BB2017.

Appendix D1. Definitions

Let f be a function that is defined on the locations x_i, y_j, z_k and times t_l of the simulation domain

$$f \doteq f(x_i, y_j, z_k, t_l). \tag{D1}$$

Decompose f into its domain horizontal mean $\overline{f}$ and the local deviation f' from this mean:

$$f \doteq \overline{f} + f' \tag{D2}$$

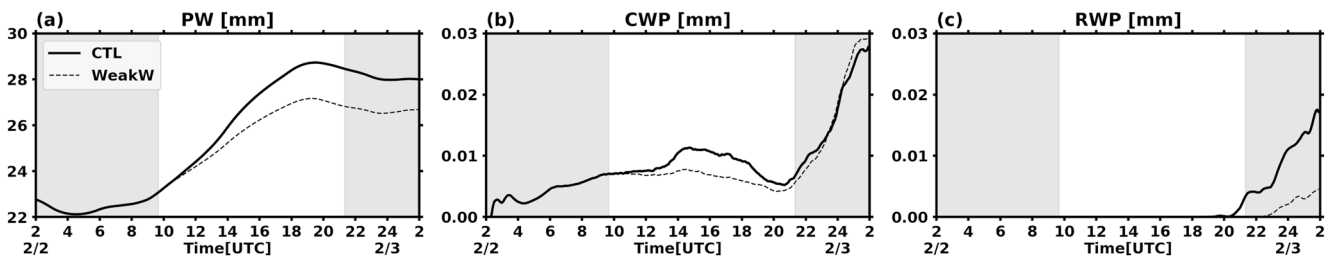

Figure C1. Time series of domain-mean: (a) Water vapor path or precipitable water, (b) Cloud water path, and (c) Rain water path from control simulation and WeakW. The sum of these three quantities are total water path, shown in Figure 3d in the main manuscript.

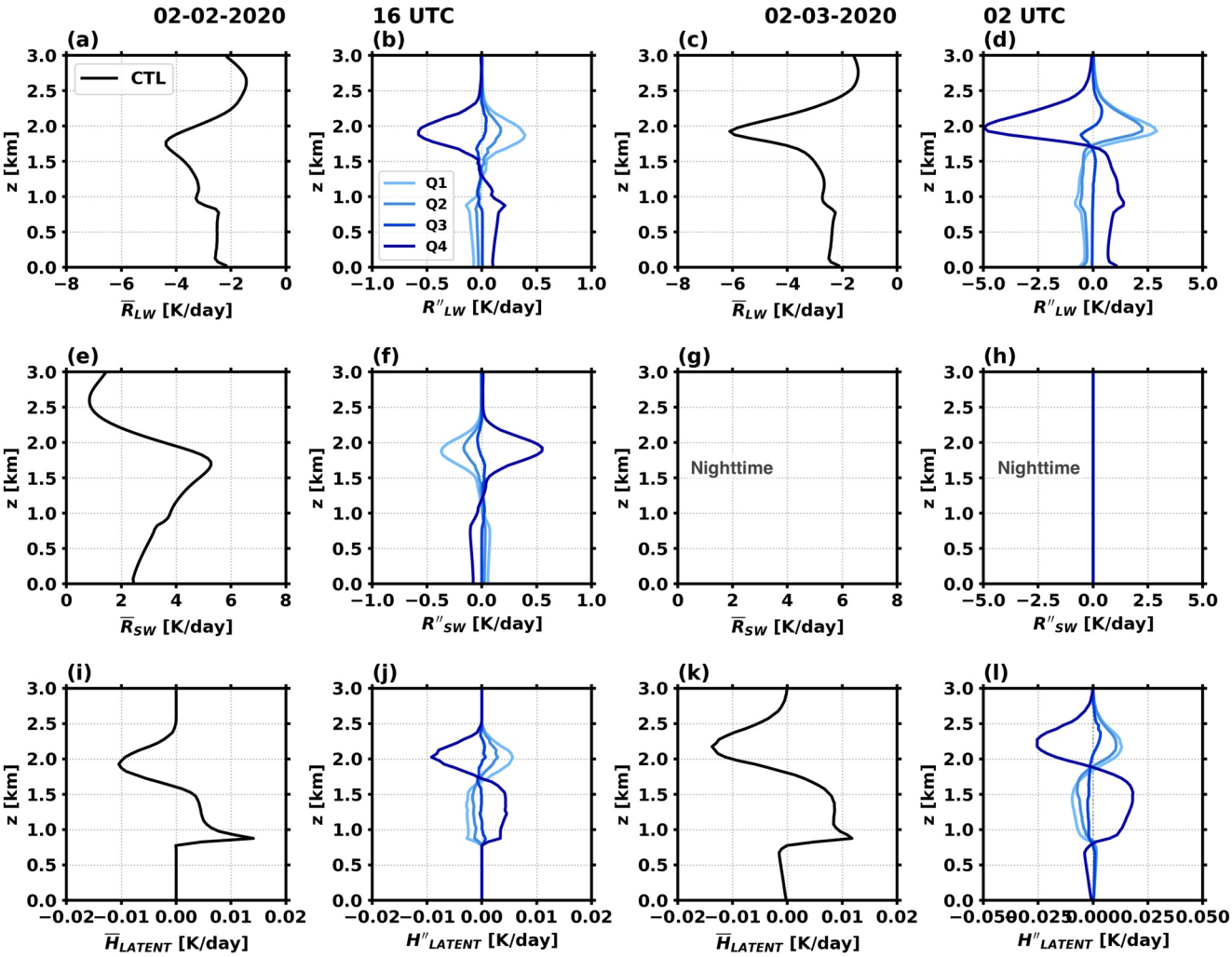

Figure C2. Vertical profiles of various variables at 16 UTC on February 2 (two left columns) and 2 UTC on February 3 (two right columns) from control simulation: (a and c) Domain-mean longwave radiative heating rate ($\overline{R}_{LW}$); (b and d) Mesoscale longwave radiative heating perturbations binned by total water path (TWP) quartiles (R''_{LW}); (e and g) Domain-mean shortwave radiative heating rate ($\overline{R}_{SW}$); (f and h) Mesoscale shortwave radiative heating perturbations binned by TWP quartiles (R''_{SW}); (i and k) Domain-mean latent heating rate due to net evaporation and condensation at the particular time step ($\overline{H}_{LATENT}$); and (j and l) Mesoscale latent heating perturbations binned by TWP quartiles (H''_{LATENT}).

Now consider a horizontal, rectangular (mesoscale) region covering $m \times n$ locations in the x and y dimensions, and let the square brackets [ ] denote the horizontal mean over the region:

$$[f] \doteq \frac{1}{mn} \sum_{m,n} f(x_i, y_j, z_k, t_l). \tag{D3}$$

(See Appendix B for how the size of the region is determined for the simulation presented in the manuscript). We decompose f into

$$f \doteq \overline{f} + f'' + f'''. \tag{D4}$$

f'' is the deviation of the region mean from the domain mean,

$$f'' \doteq [f] - \overline{f}, \tag{D5}$$

and f''' the local deviation from the region mean:

$$f''' \doteq f - [f]. \tag{D6}$$

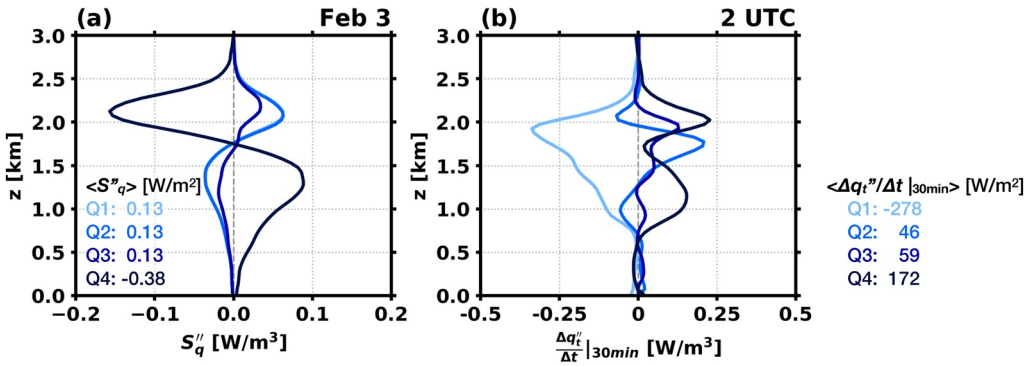

Figure C3. Vertical profiles of (a) Mesoscale perturbations of the precipitation flux divergence binned by TWP quartiles at 2 UTC on February 3, and (b) Central difference of the mesoscale total water mixing ratio perturbations (q_t'') about 2 UTC.

Appendix D2. Identities

The following identities are used in the derivation of the mesoscale tracer budget. First,

$$f' = f'' + f'''. \tag{D7}$$

Since $[f]$ is constant over the region, we find

$$[[f]] = [f]. \tag{D8}$$

Applying the horizontal mean over the region [ ] to (Equation D6) gives

$$[f'''] = 0. \tag{D9}$$

The relationships

$$[f'] = [f''], \tag{D10}$$

$$[f''] = f'', \tag{D11}$$

$$f'' = [f']. \tag{D12}$$

are elementary. Furthermore, we note that because $\overline{f}$ and f'' are constant over the region, for a function $g \doteq g(x_i, y_j, z_k, t_l)$,

$$[\overline{f}g] = \overline{f}[g], \tag{D13}$$

$$[f''g] = f''[g], \tag{D14}$$

and

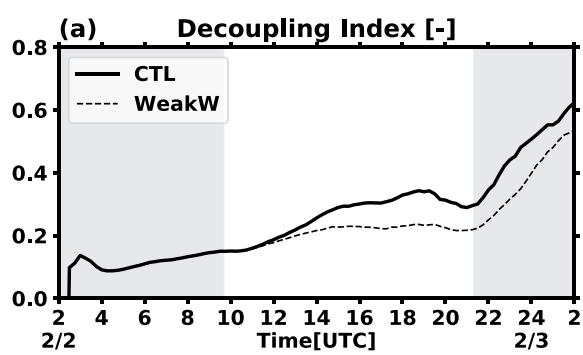

Figure C4. Time series of the domain-mean relative decoupling index from CTL and WeakW. See text for the definition of the decoupled index.

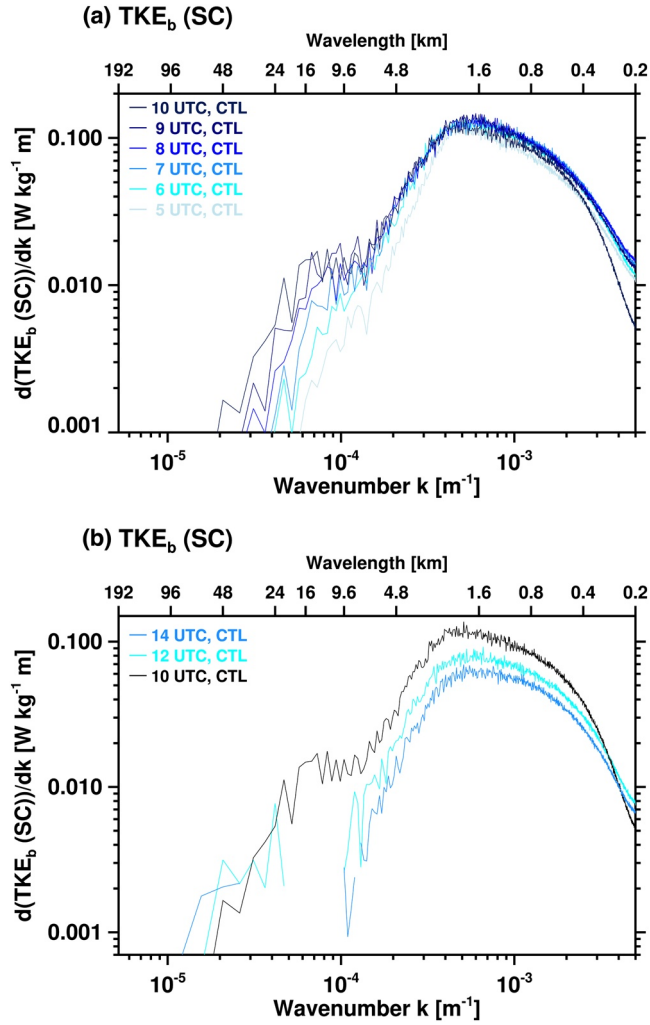

Figure C5. Spectra of buoyant turbulence kinetic energy production in the subcloud layer, or TKE$_b$ (SC), plotted (a) Hourly from 5 to 10 UTC and (b) Bi-hourly from 10 to 14 UTC.

$$[\bar{f}g'''] = \bar{f}[g'''] = 0, \tag{D15}$$

$$[f''g'''] = f''[g'''] = 0. \tag{D16}$$

From the definition of the horizontal mean over the region [ ] we obtain

$$[\nabla f] = \nabla[f]. \tag{D17}$$

The identities above hold for vectors in place of the scalars f or g. Then, because g'' and therefore $\nabla g''$ are constant over the region,

$$[\boldsymbol{v}''' \cdot \nabla g''] = [\boldsymbol{v}'''] \cdot \nabla g'' = 0. \tag{D18}$$

Based on the definition (Equation D6) and using (Equation D17),

$$[\nabla f'''] = [\nabla f] - [\nabla[f]] = [\nabla f] - [[\nabla f]] = [\nabla f] - [\nabla f] = 0. \tag{D19}$$

We did not make use of the identity $[f'''] = 0$ (Equation D9), because in general, $[g] = 0$ does not imply $[\nabla g] = 0$.

Because $\bar{\boldsymbol{v}}$ and $\boldsymbol{v}''$ are constant over the region, we obtain

$$[\overline{\boldsymbol{v}} \cdot \nabla f'''] = \overline{\boldsymbol{v}} \cdot [\nabla f'''] = 0, \tag{D20}$$

$$[\boldsymbol{v}'' \cdot \nabla f'''] = \boldsymbol{v}'' \cdot [\nabla f'''] = 0. \tag{D21}$$

Appendix D3. Derivation of the Mesoscale Tracer Budget

The continuity equation for a scalar with the mixing ratio q is

$$\frac{\partial(q\rho)}{\partial q} = -\nabla \cdot \boldsymbol{F}_q + \tilde{S}_q, \tag{D22}$$

where ρ is the air mass density, and $\boldsymbol{F}_q$ the flux and $\tilde{S}_q$ the source of q, respectively. Using the mass continuity equation and the air velocity $\boldsymbol{v} = (u, v, w)$, it can be written as

$$\frac{\partial q}{\partial t} = -\boldsymbol{v} \cdot \nabla q + S_q, \tag{D23}$$

where we set $S_q \doteq \tilde{S}_q / \rho$. Using the decomposition (Equation D2) for q and S_q, so that

$$q = \overline{q} + q', \tag{D24}$$

and

$$S_q = \overline{S}_q + S'_q \,, \tag{D25}$$

and noting that

$$\frac{\partial \overline{q}}{\partial t} = \overline{S}_q, \tag{D26}$$

we obtain

$$\frac{\partial q'}{\partial t} = -\left(\boldsymbol{v} \cdot \nabla q' + w' \frac{d\overline{q}}{dz} \right) + S'_q \,. \tag{D27}$$

Applying the horizontal mean over the region [ ] on both sides of (Equation D27), and using the identity (Equation D12) produces

$$\frac{\partial q''}{\partial t} = -\left[\boldsymbol{v} \cdot \nabla q' + w' \frac{d\overline{q}}{dz} \right] + S''_q \,, \tag{D28}$$

which simplifies to

$$\frac{\partial q''}{\partial t} = -[\boldsymbol{v} \cdot \nabla q'] - w'' \frac{d\overline{q}}{dz} + S''_q \,. \tag{D29}$$

Expanding the first term on the right hand side gives:

$$[\boldsymbol{v} \cdot \nabla q'] = [(\overline{\boldsymbol{v}} + \boldsymbol{v}'' + \boldsymbol{v}''') \cdot \nabla (q'' + q''')], \tag{D30}$$

$$= [(\overline{\boldsymbol{v}} + \boldsymbol{v}'') \cdot \nabla q''] + [\boldsymbol{v}''' \cdot \nabla q''] + [(\overline{\boldsymbol{v}} + \boldsymbol{v}'') \cdot \nabla q'''] + [\boldsymbol{v}''' \cdot \nabla q''']. \tag{D31}$$

With suitable identities, this simplifies to

$$[\boldsymbol{v} \cdot \nabla q'] = (\overline{\boldsymbol{v}} + \boldsymbol{v}'') \cdot \nabla q'' + [\boldsymbol{v}''' \cdot \nabla q''']. \tag{D32}$$

Inserting (Equation D43) into (Equation D29) produces the budget of a tracer on a (mesoscale) region

$$\frac{\partial q''}{\partial t} = -(\overline{\boldsymbol{v}} + \boldsymbol{v}'') \cdot \nabla q'' - [\boldsymbol{v}''' \cdot \nabla q'''] - w'' \frac{d\overline{q}}{dz} + S''_q \,. \tag{D33}$$

On the right hand side, the first term is associated with advection of mesoscale variability. The second term represents sub-mesoscale processes, such as individual cumulus clouds. The third term is associated with mean mesoscale vertical advection of the large scale vertical tracer gradient. The last term, the tracer source, can represent nonadvective transport, such as sedimentation. When the tracer q is total moisture, then

$$S''_q = \left(-\frac{1}{\rho} \nabla \cdot \boldsymbol{F}_p \right)'' = \left(-\frac{1}{\rho} \frac{\partial F_p}{\partial z} \right)'' \,, \tag{D34}$$

is the precipitation flux divergence, with the precipitation flux $\boldsymbol{F}_p = (0,0,F_p)$. As shown in Figures 5 and C3, for shallow cumuli that barely precipitate, the term S_q'' is much smaller than the other terms on the right hand side of Equation D33.

Appendix D4. Anelastic Approximation

In the anelastic approximation of the Navier-Stokes equations,

$$\frac{\partial \rho}{\partial t} = \nabla \cdot (\rho \boldsymbol{v}) \doteq 0, \tag{D35}$$

and

$$\frac{\partial \rho}{\partial x} \doteq \frac{\partial \rho}{\partial y} \doteq 0. \tag{D36}$$

Then, for a scalar $f = f(x_i, y_j, z_k, t_l)$, we obtain from (Equation D35)

$$\nabla \cdot (\rho \boldsymbol{v} f) = \rho \boldsymbol{v} \cdot \nabla f. \tag{D37}$$

This also holds for $f = q'''$:

$$\nabla \cdot (\rho \boldsymbol{v} q''') = \rho \boldsymbol{v} \cdot \nabla q''', \tag{D38}$$

or, equivalently,

$$\boldsymbol{v} \cdot \nabla q''' = \frac{1}{\rho} \nabla \cdot (\rho \boldsymbol{v} q'''). \tag{D39}$$

Decomposing $\boldsymbol{v} = \overline{\boldsymbol{v}} + \boldsymbol{v}'' + \boldsymbol{v}'''$ and applying the horizontal mean over the region [ ] gives

$$[(\overline{\boldsymbol{v}} + \boldsymbol{v}'' + \boldsymbol{v}''') \cdot \nabla q'''] = \frac{1}{\rho} [\nabla \cdot (\rho(\overline{\boldsymbol{v}} + \boldsymbol{v}'' + \boldsymbol{v}''') q''')]. \tag{D40}$$

On the right hand side of (Equation D40), the brackets [ ] commuted with $\frac{1}{\rho}$ because of (Equation D36). Using suitable identities, we obtain

$$[\boldsymbol{v}''' \cdot \nabla q'''] = \frac{1}{\rho} [\nabla \cdot (\rho \boldsymbol{v}''' q''')]. \tag{D41}$$

Inserting (Equation D41) into (Equation D33) yields the budget of a tracer on a (mesoscale) region in which the sub-mesoscale term was converted using the anelastic approximation:

$$\frac{\partial q''}{\partial t} = -(\overline{\boldsymbol{v}} + \boldsymbol{v}'') \cdot \nabla q'' - \frac{1}{\rho} [\nabla \cdot (\rho \boldsymbol{v}''' q''')] - w'' \frac{d\overline{q}}{dz} + S_q''. \tag{D42}$$

Expanding the second term on the right hand side of (Equation D42) with $\boldsymbol{v} = (u, v, w)$ gives

$$\frac{1}{\rho} [\nabla \cdot (\rho \boldsymbol{v}''' q''')] = \frac{\partial}{\partial x} [u''' q'''] + \frac{\partial}{\partial y} [v''' q'''] + \frac{1}{\rho} \frac{\partial}{\partial z} [\rho w q''']. \tag{D43}$$

Using the scale separation approximation (BB2017, Equation 28)

$$\nabla_h \cdot [\boldsymbol{v}''' q_t'''] = \frac{\partial}{\partial x} [u''' q'''] + \frac{\partial}{\partial y} [v''' q'''] \ll \frac{1}{\rho} \frac{\partial}{\partial z} [\rho w''' q'''] \tag{D44}$$

gives

$$\frac{\partial q''}{\partial t} = -(\overline{\boldsymbol{v}} + \boldsymbol{v}'') \cdot \nabla q'' - \frac{1}{\rho} \frac{\partial}{\partial z} [\rho w''' q'''] - w'' \frac{d\overline{q}}{dz} + S_q''. \tag{D45}$$

This is the budget of a tracer on a (mesoscale) region in the anelastic approximation derived by BB2017, in their Equation 31.

In the main manuscript, the full budget of the mesoscale tracer (Equation D42) prior to applying the scale separation approximation is used. This is because because toward the end of the simulations, the scale separation approximation or Equation D44 does not hold true.

Therefore, Equation D42 can be written as:

$$\frac{\partial q''}{\partial t} = -(\overline{\boldsymbol{v}} + \boldsymbol{v}'') \cdot \nabla q'' - \frac{1}{\rho} \frac{\partial}{\partial z} [\rho w''' q'''] - \nabla_h \cdot [\boldsymbol{v}''' q_t'''] - w'' \frac{d\overline{q}}{\boldsymbol{dz}} + S_q'', \tag{D46}$$

which is consistent with Equations 2–6 in the main manuscript.

Data Availability Statement

ERA5 data were generated using Copernicus Climate Change Service Information. Neither the European Commission or ECMWF are responsible for any use that may be made of the Copernicus information or data in this publication. Simulation outputs from this study are available at https://csl.noaa.gov/groups/csl9/datasets/data/cloud_phys/2021-Narenpitak-etal/.

Acknowledgments
This study was supported by NOAA's Climate Program Office, Climate Variability and Predictability Program (GC19-303). This is PMEL contribution number: 5239. The authors thank scientists, technicians, pilots, crew members, and everybody who made the ATOMIC and EUREC^{4}A field campaign possible. The authors thank Marat Khairoutdinov, Stony Brook University, for providing the System for Atmospheric Modeling (SAM). The authors thank Pierre Coutris, French National Centre for Scientific Research (CNRS), for providing data from the Ultra-High-Sensitivity Aerosol Spectrometer (UHSAS) and the Cloud Droplet Probe (CDP-2) on the French ATR-42 research aircraft. The authors thank Raphaela Vogel, LMD/IPSL, CNRS, Sorbonne University, Paris, France, and three anonymous reviewers whose comments helped improve the manuscript. The authors acknowledge the NOAA Research and Development High Performance Computing Program for providing computing and storage resources that have contributed to the research results reported within this study.

References

Blossey, P. N., Bretherton, C. S., Zhang, M., Cheng, A., Endo, S., Heus, T., et al. (2013). Marine low cloud sensitivity to an idealized climate change: The CGILS LES intercomparison. *Journal of Advances in Modeling Earth Systems*, *5*(2), 234–258. https://doi.org/10.1002/jame.20025

Bony, S., & Dufresne, J. L. (2005). Marine boundary layer clouds at the heart of tropical cloud feedback uncertainties in climate models. *Geophysical Research Letters*, *32*(20), 1–4. https://doi.org/10.1029/2005GL023851

Bony, S., Schulz, H., Vial, J., & Stevens, B. (2020). Sugar, gravel, fish, and flowers: Dependence of mesoscale patterns of trade-wind clouds on environmental conditions. *Geophysical Research Letters*, *47*(7), 1–9. https://doi.org/10.1029/2019gl085988

Bony, S., Stevens, B., Ament, F., Bigorre, S., Chazette, P., Crewell, S., et al. (2017). EUREC^{4}A: A field campaign to elucidate the couplings between clouds, convection and circulation. *Surveys in Geophysics*, *38*(6), 1529–1568. https://doi.org/10.1007/s10712-017-9428-0

Boucher, O., Randall, D., Artaxo, P., Bretherton, C., Feingold, G., Forster, P., & Zhang, X. Y. (2013). Clouds and aerosols. In T. F. Stocker, D. Qin, G.-K. Plattner, M. Tignor, S. K. Allen, J. Boschung (Eds.), *Climate change 2013 the physical science basis: Working group I contribution to the Fifth assessment report of the Intergovernmental Panel on Climate Change* (pp. 571–658). Cambridge University Press. https://doi.org/10.1017/CBO9781107415324.016

Bretherton, C. S., & Blossey, P. N. (2017). Understanding mesoscale aggregation of shallow cumulus convection using large-eddy simulation. *Journal of Advances in Modeling Earth Systems*, *9*(8), 2798–2821. https://doi.org/10.1002/2017MS000981

Bretherton, C. S., Blossey, P. N., & Jones, C. R. (2013). Mechanisms of marine low cloud sensitivity to idealized climate perturbations: A single-LES exploration extending the CGILS cases. *Journal of Advances in Modeling Earth Systems*, *5*(2), 316–337. https://doi.org/10.1002/jame.20019

d'Almeida, G. A., Koepke, P., & Shettle, E. P. (1991). *Atmospheric aerosols: Global climatology and radiative characteristics*. A. Deepak Pub.

Feingold, G., Walko, R. L., Stevens, B., & Cotton, W. R. (1998). Simulations of marine stratocumulus using a new microphysical parameterization scheme. *Atmospheric Research*, *47*(48), 505–528. https://doi.org/10.1016/S0169-8095(98)00058-1

Gutleben, M., Groß, S., Wirth, M., Emde, C., & Mayer, B. (2019). Impacts of water vapor on Saharan air layer radiative heating. *Geophysical Research Letters*, *46*(24), 14854–14862. https://doi.org/10.1029/2019GL085344

Hersbach, H., Bell, B., Berrisford, P., Hirahara, S., Horányi, A., Muñoz-Sabater, J., et al. (2020). The ERA5 global reanalysis. *Quarterly Journal of the Royal Meteorological Society*, *146*(730), 1999–2049. https://doi.org/10.1002/qj.3803

Holland, J. Z., & Rasmusson, E. M. (1973). Measurements of the atmospheric mass, energy, and momentum budgets over a 500-kilometer square of tropical ocean. *Monthly Weather Review*, *101*(1), 44–55. https://doi.org/10.1175/1520-0493(1973)101<0044:MOTAME>2.3.CO;2

Honnert, R., Masson, V., & Couvreux, F. (2011). A diagnostic for evaluating the representation of turbulence in atmospheric models at the kilometric scale. *Journal of the Atmospheric Sciences*, *68*(12), 3112–3131. https://doi.org/10.1175/jas-d-11-061.1

Jones, C. R., Bretherton, C. S., & Leon, D. (2011). Coupled vs. decoupled boundary layers in VOCALS-REx. *Atmospheric Chemistry and Physics*, *11*(14), 7143–7153. https://doi.org/10.5194/acp-11-7143-2011

Kazil, J., Yamaguchi, T., & Feingold, G. (2017). Mesoscale organization, entrainment, and the properties of a closed-cell stratocumulus cloud. *Journal of Advances in Modeling Earth Systems*, *9*(5), 2214–2229. https://doi.org/10.1002/2017MS001072

Khairoutdinov, M. F., & Randall, D. A. (2003). Cloud resolving modeling of the ARM summer 1997 IOP: Model formulation, results, uncertainties, and sensitivities. *Journal of the Atmospheric Sciences*, *60*(4), 607–625. https://doi.org/10.1175/1520-0469(2003)060<0607:CRMOTA>2.0.CO;2

Lamer, K., Kollias, P., & Nuijens, L. (2015). Observations of the variability of shallow trade wind cumulus cloudiness and mass flux. *Journal of Geophysical Research: Atmospheres*, *120*(12), 6161–6178. https://doi.org/10.1002/2014JD022950

Mieslinger, T., Horváth, Á., Buehler, S. A., & Sakradzija, M. (2019). The dependence of shallow cumulus macrophysical properties on large-scale meteorology as observed in ASTER imagery. *Journal of Geophysical Research: Atmospheres*, *124*(21), 11477–11505. https://doi.org/10.1029/2019JD030768

Mlawer, E. J., Taubman, S. J., Brown, P. D., Iacono, M. J., & Clough, S. A. (1997). Radiative transfer for inhomogeneous atmospheres: RRTM, a validated correlated-k model for the longwave. *Journal of Geophysical Research*, *102*(D14), 16663–16682. https://doi.org/10.1029/97JD00237

Narenpitak, P., & Bretherton, C. S. (2019). Understanding negative subtropical shallow cumulus cloud feedbacks in a near-global aquaplanet model using limited area cloud-resolving simulations. *Journal of Advances in Modeling Earth Systems*, *11*(6), 1600–1626. https://doi.org/10.1029/2018MS001572

Nuijens, L., Medeiros, B., Sandu, I., & Ahlgrimm, M. (2015). Observed and modeled patterns of covariability between low-level cloudiness and the structure of the trade-wind layer. *Journal of Advances in Modeling Earth Systems*, *7*(4), 1741–1764. https://doi.org/10.1002/2015MS000483

Nuijens, L., Serikov, I., Hirsch, L., Lonitz, K., & Stevens, B. (2014). The distribution and variability of low-level cloud in the North Atlantic trades. *Quarterly Journal of the Royal Meteorological Society*, *140*(684), 2364–2374. https://doi.org/10.1002/qj.2307

Pincus, R., Fairall, C. W., Bailey, A., Chen, H., Chuang, P. Y., de Boer, G., et al. (2021). Observations from the NOAA P-3 aircraft during ATOMIC. *Earth System Science Data Discussions*, *13*(7), 3281–3296. https://doi.org/10.5194/essd-2021-11

Quinn, P. K., Thompson, E., Coffman, D. J., Baidar, S., Bariteau, L., Bates, T. S., et al. (2020). Measurements from the RV Ronald H. Brown and related platforms as part of the Atlantic Tradewind Ocean-Atmosphere Mesoscale Interaction Campaign (ATOMIC). *Earth System Science Data Discussions*, *13*, 1–41. https://doi.org/10.5194/essd-2020-331

Rasp, S., Schulz, H., Bony, S., & Stevens, B. (2020). Combining crowd-sourcing and deep learning to explore the meso-scale organization of shallow convection. *Bulletin of the American Meteorological Society*, *101*(11), E1980–E1995. https://doi.org/10.1175/BAMS-D-19-0324.1

Rauber, R. M., Stevens, B., Ochs, H. T., Knight, C., Albrecht, B. A., Blyth, A. M., et al. (2007). Rain in shallow cumulus over the ocean: The Rico campaign. *Bulletin of the American Meteorological Society*, *88*(12), 1912–1928. https://doi.org/10.1175/BAMS-88-12-1912

Rolph, G., Stein, A., & Stunder, B. (2017). Real-time environmental applications and display system: READY. *Environmental Modelling & Software*, *95*, 210–228. https://doi.org/10.1016/j.envsoft.2017.06.025

Seifert, A., & Heus, T. (2013). Large-eddy simulation of organized precipitating trade wind cumulus clouds. *Atmospheric Chemistry and Physics*, *13*(11), 5631–5645. https://doi.org/10.5194/acp-13-5631-2013

Siebesma, A. P., Bretherton, C. S., Brown, A., Chlond, A., Cuxart, J., Duynkerke, P. G., et al. (2003). A large eddy simulation intercomparison study of shallow cumulus convection. *Journal of the Atmospheric Sciences*, *60*(10), 1201–1219. https://doi.org/10.1175/1520-0469(2003)60<1201:ALESIS>2.0.CO;2

Stein, A. F., Draxler, R. R., Rolph, G. D., Stunder, B. J. B., Cohen, M. D., & Ngan, F. (2015). NOAA's HYSPLIT atmospheric transport and dispersion modeling system. *Bulletin of the American Meteorological Society*, *96*(12), 2059–2077. https://doi.org/10.1175/BAMS-D-14-00110.1

Stevens, B., Bony, S., Brogniez, H., Hentgen, L., Hohenegger, C., Kiemle, C., et al. (2020). Sugar, gravel, fish and flowers: Mesoscale cloud patterns in the trade winds. *Quarterly Journal of the Royal Meteorological Society*, *146*(726), 141–152. https://doi.org/10.1002/qj.3662

Stevens, B., Bony, S., Farrell, D., Ament, F., Blyth, A., Fairall, C., & Zöger, M. (2021). EUREC^{4}A. *Earth System Science Data Discussions*, *13*(8), 4067–4119. https://doi.org/10.5194/essd-2021-18

vanZanten, M. C., Stevens, B., Nuijens, L., Siebesma, A. P., Ackerman, A. S., Burnet, F., et al. (2011). Controls on precipitation and cloudiness in simulations of trade-wind cumulus as observed during RICO. *Journal of Advances in Modeling Earth Systems*, *3*(2). https://doi.org/10.1029/2011MS000056

Vial, J., Vogel, R., Bony, S., Stevens, B., Winker, D. M., Cai, X., et al. (2019). A new look at the daily cycle of trade wind cumuli. *Journal of Advances in Modeling Earth Systems*, *11*(10), 3148–3166. https://doi.org/10.1029/2019MS001746

Vogel, R., Bony, S., & Stevens, B. (2020). Estimating the shallow convective mass flux from the subcloud-layer mass budget. *Journal of the Atmospheric Sciences*, *77*(5), 1559–1574. https://doi.org/10.1175/jas-d-19-0135.1

Zelinka, M. D., Zhou, C., & Klein, S. A. (2016). Insights from a refined decomposition of cloud feedbacks. *Geophysical Research Letters*, *43*, 9259–9269. https://doi.org/10.1002/2016GL069917

Zhang, M., Bretherton, C. S., Blossey, P. N., Austin, P. H., Bacmeister, J. T., Bony, S., et al. (2013). CGILS: Results from the first phase of an international project to understand the physical mechanisms of low cloud feedbacks in single column models. *Journal of Advances in Modeling Earth Systems*, *5*(4), 826–842. https://doi.org/10.1002/2013MS000246

Zuidema, P., Torri, G., Muller, C., & Chandra, A. (2017). A survey of precipitation-induced atmospheric cold pools over oceans and their interactions with the larger-scale environment. *Surveys in Geophysics*, *38*(6), 1283–1305. https://doi.org/10.1007/s10712-017-9447-x